



Physical Properties of Hyperluminous, Dust-obscured Quasars at $z \approx 3$: Multiwavelength Spectral Energy Distribution Analysis and Cold Gas

Downloaded from: <https://research.chalmers.se>, 2025-12-04 20:43 UTC

Citation for the original published paper (version of record):

Sun, W., Fan, L., Han, Y. et al (2024). Physical Properties of Hyperluminous, Dust-obscured Quasars at $z \approx 3$: Multiwavelength Spectral Energy Distribution Analysis and Cold Gas Content Revealed by ALMA. *Astrophysical Journal*, 964(1). <http://dx.doi.org/10.3847/1538-4357/ad22e3>

N.B. When citing this work, cite the original published paper.



Physical Properties of Hyperluminous, Dust-obscured Quasars at $z \sim 3$: Multiwavelength Spectral Energy Distribution Analysis and Cold Gas Content Revealed by ALMA

Weibin Sun (孙卫斌)^{1,2}, Lulu Fan (范璐璐)^{1,2,3}, Yunkun Han (韩云坤)^{4,5,6}, Kirsten K. Knudsen⁷,
Guangwen Chen (陈广文)^{1,2}, and Hong-Xin Zhang (张红欣)^{1,2}

¹ CAS Key Laboratory for Research in Galaxies and Cosmology, Department of Astronomy, University of Science and Technology of China, Hefei 230026, People's Republic of China; llfan@ustc.edu.cn

² School of Astronomy and Space Science, University of Science and Technology of China, Hefei 230026, People's Republic of China

³ Deep Space Exploration Laboratory, Hefei 230088, People's Republic of China

⁴ Yunnan Observatories, Chinese Academy of Sciences, 396 Yangfangwang, Guandu District, Kunming 650216, People's Republic of China

⁵ Center for Astronomical Mega-Science, Chinese Academy of Sciences, 20A Datun Road, Chaoyang District, Beijing 100012, People's Republic of China

⁶ Key Laboratory for the Structure and Evolution of Celestial Objects, Chinese Academy of Sciences, 396 Yangfangwang, Guandu District, Kunming 650216, People's Republic of China

⁷ Department of Space, Earth and Environment, Chalmers University of Technology, Onsala Space Observatory, SE-439 92 Onsala, Sweden

Received 2023 October 17; revised 2024 January 22; accepted 2024 January 26; published 2024 March 20

Abstract

We present a UV to millimeter spectral energy distribution (SED) analysis of 16 hyperluminous, dust-obscured quasars at $z \sim 3$, selected by the Wide-field Infrared Survey Explorer. We aim to investigate the physical properties of these quasars, with a focus on their molecular gas content. We decompose the SEDs into three components: stellar, cold dust, and active galactic nucleus (AGN). By doing so, we are able to derive and analyze the relevant properties of each component. We determine the molecular gas mass from CO line emission based on Atacama Large Millimeter/submillimeter Array (ALMA) observations. By including ALMA observations in the multiwavelength SED analysis, we derive the molecular gas fractions, gas depletion timescales, and star formation efficiencies (SFEs). Their sample median and 16th–84th quartile ranges are $f_{\text{gas}} \sim 0.33^{+0.33}_{-0.17}$, $t_{\text{depl}} \sim 39^{+85}_{-28}$ Myr, and $\text{SFE} \sim 297^{+659}_{-195}$ K km s^{−1} pc^{−2}, respectively. Compared to main-sequence galaxies, they have lower molecular gas content and higher SFEs, similar to quasars in the literature. This suggests that the gas in these quasars is rapidly depleted, likely as the result of intense starburst activity and AGN feedback. The observed correlations between these properties and the AGN luminosities further support this scenario. Additionally, we infer the black hole to stellar mass ratio and black hole mass growth rate, which indicate significant central black hole mass assembly over short timescales. Our results are consistent with the scenario that our sample represents a short transition phase toward unobscured quasars.

Unified Astronomy Thesaurus concepts: Active galaxies (17); High-redshift galaxies (734); Starburst galaxies (1570); Quasars (1319)

1. Introduction

The coevolution between the central supermassive black hole (SMBH) and host galaxy is now widely acknowledged (Kormendy & Ho 2013). This is evidenced by the tight correlation between the mass of central SMBHs and the stellar bulge masses in galaxies (e.g., Magorrian et al. 1998; Ferrarese & Ford 2005). In one of the most popular coevolution scenarios, gas-rich major galaxy mergers trigger intense starbursts, provide the fuel for central SMBH accretion, and trigger active galactic nucleus (AGN) activity delayed after the triggering of starbursts (Hopkins et al. 2008). This stage of AGN–starburst composite systems often leads to the observation of galaxies as dust-obscured quasars. The galaxies will evolve to unobscured quasars after the accreting SMBH experienced a feedback phase, which clears the dust and gas in the galaxy in the form of powerful outflowing winds (see Fabian 2012; Somerville & Davé 2015, for recent reviews). During this evolutionary sequence first presented by Sanders et al. (1988), dust-obscured quasars have been identified as

essential links between starbursts and unobscured quasars. They serve a critical role in the rapid assembly of both the SMBH and galaxy mass, as well as in AGN feedback (Hickox & Alexander 2018). Evidence from both observations and theoretical models have suggested that the efficiency of galaxy-scale outflows increases with quasar bolometric luminosity (see, e.g., Heckman & Best 2014; Hopkins et al. 2016; Fiore et al. 2017; García-Burillo et al. 2021). Therefore, luminous, obscured quasars are good candidates for investigating the interplay between host galaxies and their central SMBHs.

The Wide-field Infrared Survey Explorer (WISE; Wright et al. 2010) has revealed an important population of luminous, dust-obscured galaxies (DOGs) at $z \sim 3$ by selecting sources that are strongly detected at 12 and 22 μm , but weakly or not detected at 3.4 and 4.6 μm (Eisenhardt et al. 2012). A variety of follow-up studies utilizing different techniques have been carried out. Multiband spectral energy distribution (SED) analyses have played an essential role in the study of these high-redshift objects. Through the construction of median IR SEDs, it has been revealed that these galaxies exhibit a high mid-infrared (MIR) to submillimeter luminosity ratio, elevated dust temperatures, and extraordinary bolometric luminosities over $10^{13} L_{\odot}$ (Wu et al. 2012). The number density of these luminous, DOGs is comparable to that of equally luminous



Original content from this work may be used under the terms of the [Creative Commons Attribution 4.0 licence](https://creativecommons.org/licenses/by/4.0/). Any further distribution of this work must maintain attribution to the author(s) and the title of the work, journal citation and DOI.

Table 1
Sample Properties

Source Name (1)	R.A. _{WISE} (J2000) (2)	Decl. _{WISE} (J2000) (3)	Redshift (4)	$\log L_{\text{IR}}^{\text{t}}$ $\log(L_{\odot})$ (5)	$\log L_{\text{IR}}^{\text{cd}}$ $\log(L_{\odot})$ (6)
W0126–0529 ^a	01:26:11.96	–05:29:09.6	2.937	13.95 ± 0.01	13.90 ± 0.02
W0134–2922	01:34:35.71	–29:22:45.4	3.047	13.97 ± 0.03	13.15 ± 0.03
W0149+2350	01:49:46.16	+23:50:14.6	3.228	13.90 ± 0.04	13.11 ± 0.07
W0220+0137	02:20:52.12	01:37:11.60	3.122	14.07 ± 0.02	13.63 ± 0.04
W0248+2705	02:48:58.81	27:05:29.80	2.210	13.45 ± 0.05	13.11 ± 0.07
W0410–0913	04:10:10.60	–09:13:05.2	3.592	14.12 ± 0.03	13.84 ± 0.03
W0533–3401	05:33:58.44	–34:01:34.5	2.904	13.94 ± 0.04	13.50 ± 0.04
W0615–5716	06:15:11.07	–57:16:14.6	3.399	14.13 ± 0.02	13.33 ± 0.14
W1248–2154	12:48:15.21	–21:54:20.4	3.318	14.15 ± 0.02	13.18 ± 0.07
W1603+2745	16:03:57.39	27:45:53.30	2.633	13.61 ± 0.02	13.32 ± 0.04
W1814+3412	18:14:17.30	34:12:25.00	2.452	13.72 ± 0.03	13.12 ± 0.07
W2054+0207	20:54:25.69	02:07:11.00	2.520	13.66 ± 0.05	13.16 ± 0.06
W2201+0226	22:01:23.39	02:26:21.80	2.877	13.84 ± 0.03	13.73 ± 0.02
W2210–3507	22:10:11.87	–35:07:20.0	2.814	13.93 ± 0.02	13.47 ± 0.02
W2238+2653	22:38:10.20	26:53:19.80	2.405	13.79 ± 0.03	13.48 ± 0.04
W2246–0526	22:46:07.57	05:26:35.00	4.593	14.46 ± 0.02	13.73 ± 0.04
W2305–0039	23:05:25.88	–00:39:25.7	3.106	13.97 ± 0.02	13.61 ± 0.03

Notes. Column (1): source name. Columns (2) and (3): WISE coordinates from the AllWISE database. Column (4): spectroscopic redshifts from Wu et al. (2012) and Tsai et al. (2015). Columns (5) and (6): IR luminosity of the AGN torus and cold dust emission derived by IR decomposition, respectively, as reported in Fan et al. (2016b).

^a W0126–0529 has been excluded from our sample for its ambiguous redshift identification.

type 1 quasars (Assef et al. 2015). These galaxies represent an exceedingly rare class of DOGs, now commonly referred to as hot, dust-obscured galaxies (Hot DOGs). Further investigations have shown that the IR SEDs of the most luminous Hot DOGs are dominated by hot dust at a temperature exceeding 450 K (Tsai et al. 2015), and their IR SEDs can be decomposed through two-component, AGN–starburst SED fitting (Fan et al. 2016b, 2017, 2018). UV–optical spectral analyses of Hot DOGs found black hole masses $\sim 10^6 M_{\odot}$, which are accreting near or above the Eddington limit and also host powerful ionized outflows (Wu et al. 2012; Tsai et al. 2018; Wu et al. 2018; Finnerty et al. 2020; Jun et al. 2020). Millimeter interferometric observations like those obtained with the Atacama Large Millimeter/submillimeter Array (ALMA) of several Hot DOGs revealed a highly turbulent interstellar medium (ISM) and also provide evidence of possible molecular outflows (Wu et al. 2014; Díaz-Santos et al. 2016, 2018; Fan et al. 2018, 2019; Penney et al. 2020; Díaz-Santos et al. 2021). The X-ray observations of Hot DOGs consistently find high column densities that are close to Compton thick (Stern et al. 2014; Piconcelli et al. 2015; Assef et al. 2016; Ricci et al. 2017; Vito et al. 2018; Zappacosta et al. 2018; Assef et al. 2020). The environments where Hot DOGs reside were found to be significantly overdense (Jones et al. 2015; Silva et al. 2015; Jones et al. 2017; Penney et al. 2019; Ginolfi et al. 2022; Luo et al. 2022; Zewdie et al. 2023). All results are generally consistent with the merger-driven coevolution scenario.

SED fitting is an effective method for decomposing emissions between star formation and AGN (Sokol et al. 2023). Some widely used SED fitting codes, including SED3FIT (Berta et al. 2013), CIGALE (Boquien et al. 2019; Yang et al. 2022), and BayeSED (Han & Han 2012, 2014, 2019) have been proven to be efficient tools for exploring AGN–starburst systems, and AGN models are constantly evolving and becoming more and more accurate and realistic (Fritz et al. 2006; Nenkova et al. 2008a, 2008b; Hönig &

Kishimoto 2010; Siebenmorgen et al. 2015; Stalevski et al. 2016; Hönig & Kishimoto 2017). At high redshift, it is hard to resolve the central AGN emission from the host galaxy. SED observations, modeling, and fitting are indispensable to investigate the physical properties of these high-redshift AGNs and their host galaxies (e.g., Merloni et al. 2010; Bongiorno et al. 2014; Suh et al. 2019; López et al. 2023).

Molecular gas, predominantly traced by carbon monoxide (CO) emission lines, acts as the fuel for both star formation and black hole accretion. Additionally, it plays an important role in energy feedback from AGN (e.g., Feruglio et al. 2017; Bischetti et al. 2019; Fluetsch et al. 2019). Investigations of the molecular gas content (M_{H_2}) in quasars, coupled with other observables such as SED-derived dust masses (M_{dust}), stellar masses (M_{\star}), and star formation rates (SFRs), provide valuable insights into the physical processes driving the coevolution of galaxies and SMBHs (e.g., Brusa et al. 2015; Banerji et al. 2017; Kakkad et al. 2017; Brusa et al. 2018; Perna et al. 2018; Bischetti et al. 2021). However, for “Cosmic Noon” ($z \sim 2\text{--}3$) when both star formation and black hole accretion activity in the Universe peaked (Shapley 2011), there is a lack of systematic investigation into the molecular gas properties of luminous quasars, primarily limited to analyses of individual sources or relatively small sample sizes.

To investigate systematically the physical properties of Hot DOGs at $z \sim 3$, particularly their cold gas content, we conduct a comprehensive UV to millimeter SED analysis of a subsample of 16 Hot DOGs selected from Fan et al. (2016b). Table 1 lists the properties of these Hot DOGs, as reported in Fan et al. (2016b). This subsample has ALMA observations of CO emission lines, which were used to constrain their molecular gas content. This study represents the largest sample of high-redshift, luminous, obscured quasars so far in this kind of study. We derived the properties of the stellar, cold dust, AGN, and gas components and calculated their relative values (e.g., molecular gas fraction $f_{\text{gas}} = M_{\text{H}_2} / (M_{\text{H}_2} + M_{\star})$ and star

Table 2
Summary of the ALMA Observations

Source Name	Line	Date (DD-MM-YYYY)	Flux & Bandpass Calibrator	Gain Calibrator	σ^a (mJy beam ⁻¹)	Beam (arcsec \times arcsec)
W0126–0529	CO(3–2)	02-01-2018	J0006–0623	J0141–0202	0.45	0.61×0.52 , 82°4
W0134–2922 ^b	CO(4–3)	12-12-2017	J2357–5311	J0120–2701	0.11	0.39×0.27 , –63°1
		13-12-2017	J2357–5311	J0120–2701		
W0248+2705	CO(4–3)	10-01-2018	J0238+1636	J0237+2848	0.42	0.58×0.56 , 23°9
W0533–3401	CO(3–2)	20-12-2017	J0538–4405	J0522–3627	0.32	0.60×0.51 , –78°9
W0615–5716 ^b	CO(4–3)	07-12-2017	J0519–4546	J0550–5732	0.11	0.32×0.28 , –45°8
W1248–2154 ^b	CO(4–3)	28-01-2018	J1337–1257	J1245–1616	0.12	0.50×0.48 , 46°9
W1603+2745	CO(3–2)	24-01-2018	J1550+0527	J1619+2247	0.16	1.09×0.74 , –19°7
		30-09-2018	J1550+0527	J1619+2247		
W1814+3412	CO(4–3)	10-01-2018	J1751+0939	J1753+2848	0.32	0.61×0.46 , 22°6
W2054+0207	CO(4–3)	20-01-2018	J2134–0153	J2101+0341	0.23	0.74×0.52 , 50°8
W2201+0226	CO(3–2)	01-01-2018	J2148+0657	J2156–0037	0.39	0.62×0.51 , –46°7
W2210–3507	CO(3–2)	01-01-2018	J2258–2758	J2151–3027	0.35	0.68×0.60 , –58°4
W2238+2653	CO(4–3)	01-10-2018	J2253+1608	J2236+2828	0.35	0.72×0.51 , –4°3
W2305–0039 ^b	CO(4–3)	10-12-2017	J0006–0623	J2301–0158	0.12	0.39×0.32 , 60°5

Notes.

^a Sensitivity in a 100 km s⁻¹ velocity bin.

^b From project 2017.1.00358.S; we note that W1248–2154 was observed in both projects, however we use these data as they are deeper.

formation efficiency; SFE), further testing the role of Hot DOGs in massive galaxy and SMBH coevolution. In Section 2, we present details of the ALMA observations and the subsequent data analysis. Section 3 covers the construction of our multiwavelength SEDs and the SED modeling approach we used. Results and discussions are described in Sections 4 and 5, respectively. Finally, in Section 6, we summarize our findings and draw conclusions. Throughout this work, we assume a Lambda cold dark matter (Λ CDM) cosmology (see Komatsu et al. 2011) with $H_0 = 70$ km s⁻¹ Mpc⁻¹, $\Omega_M = 0.3$, and $\Omega_\Lambda = 0.7$.

2. ALMA Observations and Data Analysis

Observations were carried out with ALMA using the Band 3 and Band 4 receivers during Cycle 5. Most of our sample sources were observed in our project 2017.1.00441.S (PI: L. Fan). A few sources were allocated to a different project and are available in the ALMA archive (2017.1.00358.S), and we also include these observations.⁸ Table 2 summarizes the details of the observations, including a list of calibrators. We note that while the observations in 2017.1.00441.S used a spectral setup for the spectral window (spw) of the sideband that was predicted to include the emission line (and continuum mode for the spectral windows of the other sideband), project 2017.1.00358.S used a continuum setup for all spectral windows.

Reduction, calibration, and imaging were done using the Common Astronomy Software Application (CASA;⁹ McMullin et al. 2007). The pipeline-reduced data delivered from the observatory was of sufficient quality such that no additional flagging and further calibration were necessary. The pipeline includes the steps required for a standard reduction and calibration, such as flagging, bandpass calibration, as well as flux and gain calibration. A conservative estimate of the uncertainty of the absolute flux calibration is 10%.

The data were imaged both as a continuum and spectral cube using natural weighting. The CASA task `uvcontsub` was used to subtract the continuum from the *uv* data for sources for which the continuum was detected. A continuum image was produced combining all spectral windows, while a spectral cube was constructed for the spectral windows tuned to the redshifted CO line. The rms sensitivity and the synthesized beam size achieved by imaging with a natural weighting scheme are given in Table 2.

3. Multiwavelength Data and Spectral Energy Distribution Fitting

3.1. UV to Millimeter Spectral Energy Distribution Data

To decompose the host galaxy emission from the central AGN and estimate their physical properties, such as stellar mass (M_*) and SFR, we constructed UV to millimeter SEDs for all objects in our sample. Various photometry catalogs were retrieved. 13 Hot DOGs in our sample have optical to near-infrared (NIR) broadband photometric data from different surveys, including the first public data release of the Dark Energy Survey (DES DR1; Abbott et al. 2018)¹⁰ in the *g*, *r*, *i*, *z*, and *Y* bands; the seventh public data release of the Dark Energy Camera Legacy Survey (DECaLS DR7; Dey et al. 2019)¹¹ in the *g*, *r*, and *z* bands; the third Data Release of the Beijing–Arizona Sky Survey (BASS DR3; Zou et al. 2019)¹² in the *g*, *r*, and *z* bands; and the fourth Data Release of Kilo-Degree Survey (KiDs DR4; Kuijken et al. 2019)¹³ together with data from the Visible and Infrared Survey Telescope for Astronomy (VISTA) Kilo-degree Infrared Galaxy (VIKING) Survey (Edge et al. 2013) in the *u*, *g*, *r*, *i*, *Z*, *Y*, *J*, *H*, and *K_s* bands; Two Micron All Sky Survey (2MASS) photometry from NED¹⁴ in the *H* and *K_s* bands, and from the Sloan Digital Sky Survey (SDSS).¹⁵

¹⁰ <https://des.ncsa.illinois.edu/releases/dr1/>

¹¹ <https://www.legacysurvey.org/dr7/>

¹² <http://explore.china-vo.org/data/bassdr3coadd/>

¹³ <http://kids.strw.leidenuniv.nl/DR4/>

¹⁴ <https://ned.ipac.caltech.edu/>

¹⁵ <https://www.sdss.org/dr15/>

⁸ We note that 2017.1.00358.S has more sources; however, as these were not part of our original sample, we do not include them in this analysis.

⁹ <https://casa.nrao.edu>

The three remaining Hot DOGs, namely W0248+2705, W0615–5716, and W1248–2154, currently lack optical–NIR data. The WISE W1 and W2 flux densities were obtained through aperture photometry on the WISE images¹⁶ (from the unWISE catalog; Lang 2014; Meisner et al. 2017), and the errors were estimated based on the inverse variance images. The optical–NIR photometry catalog of our sample is shown in Table 3. The WISE W3 and W4 photometry data were obtained from the ALLWISE Data Release (Cutri et al. 2013). For the far-infrared (FIR) to millimeter photometry, because of the sample selection in Fan et al. (2016b), all Hot DOGs have Herschel Photoconductor Array Camera and Spectrometer (PACS; Poglitsch et al. 2010) observations at 70 and 160 μm and Spectral and Photometric Imaging REceiver (SPIRE; Griffin et al. 2010) observations at 250, 350, and 500 μm (Pilbratt et al. 2010). Part of our sample have James Clerk Maxwell Telescope (JCMT) SCUBA-2 observations (Jones et al. 2014), as well as CSO SHARC-II observations at 850 μm , CSO Bolocam observations at 1.1 mm (Wu et al. 2012), and Submillimeter Array (SMA) observations at 1.3 mm (Wu et al. 2014). The IR broadband photometry at wavelengths ranging from 12 μm to the millimeter band were directly collected from their parent samples as reported in Fan et al. (2016b). The ALMA continuum observations at rest-frame 3 mm have been included to constrain the cold dust component more accurately.

3.2. SED Analysis

The UV to millimeter SED fitting in our study was conducted with the latest version of BayeSED (Han & Han 2012, 2014, 2019),¹⁷ namely BayeSED v3.0. This new version has improved accuracy and speed relative to the original stellar population synthesis algorithm and has been tested with mock galaxies to show good quality and speed for parameter estimation of galaxies (Han et al. 2023). For SED models given as a SED library, principal component analysis is employed to reduce memory usage. Then, interpolation between the SED models is conducted with artificial neural networks or the K-nearest neighbors algorithm to allow a fast and continuous sampling of high-dimensional parameter space. Finally, the MultiNest algorithm is employed to sample the parameter space and calculate the posterior probability distribution of the parameters.

The SED of each galaxy in our sample was decomposed into three components: stellar, cold dust, and central AGN. The stellar emission was modeled by using the Bruzual & Charlot (2003) simple stellar population library with a Chabrier (2003) initial mass function (IMF) and an exponential declining star formation history (SFH). The Calzetti et al. (2000) dust attenuation law was used, and the energy of stellar emission absorbed by cold dust was assumed to be totally reemitted in the IR band. This assumption can break the degeneracy in the UV and optical bands by the complement of IR photometry (da Cunha et al. 2008; Buat et al. 2014), and stellar population properties can be more robustly constrained. The cold dust emission was modeled conventionally as a graybody, which was defined as $S_\lambda \propto (1 - e^{-\frac{\lambda_0}{\lambda}})^\beta B_\lambda(T_{\text{dust}})$, where $\lambda_0 = 125 \mu\text{m}$ and the dust temperature T_{dust} and the emissivity index β are two free parameters in the SED fitting. The CLUMPY torus model

(Nenkova et al. 2008a, 2008b)¹⁸ has significantly advanced the modeling of IR emission in various AGN samples (Ramos Almeida & Ricci 2017), and has been utilized to model the UV–IR emission of the central AGN of our samples. Six parameters are employed in the CLUMPY model to describe the geometry and physical properties of the CLUMPY torus. The SED analysis method employed in this study is consistent with that used in a previous work by Fan et al. (2019), who presented a comprehensive analysis of W0533–3401. However, we have restricted the T_{dust} parameter to the range 30–50 K to address AGN contamination in the FIR, as discussed in Section 5.4. The 12 free parameters used in the fitting process are listed in Table 3 of Fan et al. (2019). For the three Hot DOGs without optical–NIR photometry, we excluded the stellar population component to prevent overfitting. Thus, the stellar population parameters, such as M_* , have not been estimated for these three galaxies. The upper flux density limit was taken into account by setting the corresponding flux density error to a negative value according to the convention in BayeSED.

4. Results

4.1. CO Emission Lines and Continuum

We detect significant CO(3–2) or CO(4–3) emission lines for all but four galaxies in our sample. Among the four galaxies, W0248+2705 and W1814+3412 have a tentative detection, while no emission lines were found for the other two sources. The emission lines were fitted with a single Gaussian line profile to estimate the redshift, peak flux density, line width, and integrated intensity. The results are given in Table 4. For the four nondetections, 3σ upper limits of the peak flux density and integrated intensity (assuming a line width of 300 km s^{-1}) are reported in Table 4. Galaxy centers were estimated from the moment 0 maps. Figure 1 shows the CO line spectra and moment 0 maps of our galaxies.

The continuum was detected in all but four galaxies. The continuum flux density and size were measured by fitting 2D Gaussian profile to the maps. We note that W0126–0529 has no line detection but has a clear detection of its continuum. The relevant measurements of the continuum are reported in Table 4, where nondetections are listed as 5σ upper limits.

The line luminosities L'_{CO} in units of $\text{K km s}^{-1} \text{ pc}^2$ were calculated by using an equation from Solomon & Vanden Bout (2005):

$$L'_{\text{CO}} = 3.25 \times 10^7 S_{\text{CO}} \Delta\nu \nu_{\text{obs}}^{-2} D_L^2 (1+z)^{-3}, \quad (1)$$

where $S_{\text{CO}}\Delta\nu$ is the CO line flux in units of Jy km s^{-1} , D_L is the luminosity distance in units of Mpc, and ν_{obs} is the observed frequency in units of GHz. The line emission data for W0149+2305, W0220+0137, and W0410–0913 were collected from Fan et al. (2018), and the line emission data for W2246–0526 were obtained from Díaz-Santos et al. (2018). W0126–0529 has been reobserved recently and a redshift of $z = 0.832$ (Vito et al. 2018) has been reported, suggesting that it may be classified as a low-redshift Hot DOG, similar to W1904+4853 in Li et al. (2023). An uncertain redshift might be responsible for its nondetection in our observations. Thus, we chose to discard this source from our analysis. Utilizing line ratios of $L'_{\text{CO}(3-2)}/$

¹⁶ <https://unwise.me/>
¹⁷ <https://bitbucket.org/hanyk/bayesed/>

¹⁸ http://www.pa.uky.edu/clumpy/models/clumpy_models_201410_tvavg.hdf5/

Table 3
Optical–NIR photometry

Source	<i>u</i> (μ Jy)	<i>g</i> (μ Jy)	<i>r</i> (μ Jy)	<i>i</i> (μ Jy)	<i>z</i> (μ Jy)	<i>Y</i> (μ Jy)	<i>J</i> (μ Jy)	<i>H</i> (μ Jy)	<i>Ks</i> (μ Jy)	W1 (μ Jy)	W2 (μ Jy)
W0134–2922 ^a	1.27 \pm 0.34	3.54 \pm 0.11	4.53 \pm 0.12	6.13 \pm 0.84	6.23 \pm 0.38	8.84 \pm 0.9	8.88 \pm 0.81	10.77 \pm 1.97	16.38 \pm 1.85	23.04 \pm 4.7	96.21 \pm 9.68
W0149+2350 ^b	...	0.45 \pm 0.15	1.21 \pm 0.3	...	2.57 \pm 0.44	14.47 \pm 2.09	25.88 \pm 4.78
W0220+0137 ^{c,e}	1.49 \pm 0.85	7.06 \pm 0.38	6.63 \pm 0.53	5.42 \pm 0.66	8.16 \pm 2.06	18.53 \pm 2.06	31.55 \pm 4.84
W0248+2705	10.7 \pm 4.99	30.48 \pm 10.77
W0410–0913 ^b	...	0.32 \pm 0.26	2.57 \pm 0.42	...	2.55 \pm 0.52	65.88 \pm 2.2	66.21 \pm 4.8
W0533–3401 ^c	...	4.86 \pm 0.21	7.12 \pm 0.27	9.62 \pm 0.52	13.14 \pm 1.11	11.64 \pm 3.21	35.07 \pm 1.65	72.61 \pm 3.63
W0615–5716	35.52 \pm 2.91	43.33 \pm 5.24
W1248–2154	44.42 \pm 4.59	35.48 \pm 9.35
W1603+2745 ^b	...	0.46 \pm 0.13	0.82 \pm 0.19	...	1.95 \pm 0.36	7.42 \pm 1.67	31.08 \pm 3.86
W1814+3412 ^d	...	1.33 \pm 0.2	6.51 \pm 0.57	...	7.42 \pm 0.71	8.63 \pm 3.59	15.16 \pm 7.11
W2054+0207 ^b	...	0.83 \pm 0.12	1.5 \pm 0.15	...	5.48 \pm 0.4	14.83 \pm 2.03	115.43 \pm 4.64
W2201+0226 ^b	...	0.85 \pm 0.11	1.05 \pm 0.22	...	2.34 \pm 0.68	18.2 \pm 2.17	83.29 \pm 5.01
W2210–3507 ^a	0.84 \pm 0.25	1.17 \pm 0.09	1.68 \pm 0.1	1.69 \pm 0.5	3.05 \pm 0.47	2.15 \pm 0.88	6.88 \pm 0.75	8.72 \pm 1.7	13.61 \pm 2.23	27.49 \pm 4.96	34.8 \pm 11.38
W2238+2653 ^{b,e}	1.1 \pm 0.76	1.51 \pm 0.32	2.85 \pm 0.54	5.06 \pm 0.84	5.3 \pm 2.78	27.45 \pm 1.9	59.72 \pm 4.32
W2246–0526 ^f	5.2 \pm 0.2	8.8 \pm 2.8	31.0 \pm 7.0	34.0 \pm 7.0
W2305–0039 ^{c,e}	0.59 \pm 0.47	...	1.98 \pm 0.5	3.97 \pm 0.72	6.25 \pm 2.47	22.83 \pm 2.27	44.56 \pm 5.25

Notes.

^a (*u*, *g*, *r*, *i*, *z*, *Y*, *J*, *H*, and *Ks*) band photometry from the KiDS DR4 and VIKING catalogs.

^b (*g*, *r*, and *z*) band photometry from the DECaLS DR7 catalog.

^c (*g*, *r*, *i*, *z*, and *Y*) band photometry from the DES DR1 catalog.

^d (*g*, *r*, and *z*) band photometry from the BASS DR3 catalog.

^e (*u* and *i*) band photometry from SDSS.

^f (*H* and *Ks*) bands from 2MASS photometry.

Table 4
CO and Millimeter Continuum Measurements Based on ALMA Observations

Source Name (1)	R.A. (J2000) (2)	Decl. (J2000) (3)	z_{CO} (4)	S_{peak} (mJy beam $^{-1}$) (5)	FWHM (km s $^{-1}$) (6)	I_{CO} (Jy km s $^{-1}$) (7)	ν_{cen} GHz (8)	S_{cont} (μ Jy) (9)	Size (arcsec \times arcsec) (10)
W0126–0529 ^{a,b}	<1.35	300	<0.43	93.64	462 \pm 71	0.41 \times 0.33, 30 $^\circ$
W0134–2922	01:34:35.70	–29:22:45.54	3.0572 \pm 0.0004	0.85 \pm 0.09	612 \pm 74	0.55 \pm 0.09	106.96	35 \pm 10	unresolved
W0248+2705TT	02:48:58.71	+27:05:30.08	2.1825 \pm 0.0007	1.26 \pm 0.29	551 \pm 150	0.74 \pm 0.26			
W0533–3401	05:33:58.41	–34:01:34.50	2.9024 \pm 0.0003	4.83 \pm 0.42	555 \pm 55	2.86 \pm 0.38	94.36	169 \pm 48	unresolved
W0615–5716	06:15:11.10	–57:16:14.81	3.3463 \pm 0.0007	0.54 \pm 0.08	723 \pm 115	0.42 \pm 0.09	99.70	<60	...
W1248–2154	12:48:15.20	–21:54:20.12	3.3233 \pm 0.0007	0.31 \pm 0.05	610 \pm 113	0.20 \pm 0.05	99.94	147 \pm 28	unresolved
W1603+2745	16:03:57.36	+27:45:52.95	2.6540 \pm 0.0005	1.77 \pm 0.15	1081 \pm 103	2.04 \pm 0.26	100.88	94 \pm 27	extended
W1814+3412 TT	18:14:17.27	+34:12:24.45	2.4568 \pm 0.0004	0.76 \pm 0.19	254 \pm 74	0.21 \pm 0.08	139.12	<125	...
W2054+0207	20:54:25.68	+02:07:11.56	2.5323 \pm 0.0002	4.87 \pm 0.31	457 \pm 34	2.37 \pm 0.23	136.61	212 \pm 52	0.55 \times 0.41, 165 $^\circ$
W2201+0226	22:01:23.38	+02:26:21.87	2.8752 \pm 0.0003	15.0 \pm 0.87	691 \pm 46	11.0 \pm 0.97	94.87	119 \pm 36	unresolved
W2210–3507 ^a	<1.1	300	<0.34	96.35	<130	...
W2238+2653	22:38:10.19	+26:53:20.01	2.3987 \pm 0.0002	13.0 \pm 0.52	698 \pm 32	9.65 \pm 0.58	141.02	484 \pm 82	0.77 \times 0.32, 170 $^\circ$
W2305–0039	23:05:25.86	–00:39:25.35	3.1107 \pm 0.0002	5.79 \pm 0.23	570 \pm 26	3.51 \pm 0.21	107.246	220 \pm 22	0.22 \times 0.16, 177 $^\circ$

Notes. Column (1): source names. Columns (2) and (3): positions derived from the moment 0 maps. Column (4): redshift based on the CO (3–2) emission line. Columns (5), (6), and (7): peak flux density, line width, and line intensity based on the Gaussian line profile, respectively. Columns (8), (9), and (10): frequency, flux density, and size of the continuum detections based on a 2D Gaussian profile fitting, respectively. TT: tentative line detection.

^a 3σ upper limits of the CO line intensity are calculated assuming a line width of 300 km s $^{-1}$ and the 5σ upper limits of the continuum are calculated assuming the source is compact.

^b Continuum position at (01:26:11.95, –05:29:09.31).

$L'_{\text{CO}(1-0)} = 0.97$ and $L'_{\text{CO}(4-3)}/L'_{\text{CO}(1-0)} = 0.87$, as recommended for QSOs (Carilli & Walter 2013), we derived the CO(1–0) line luminosities. We note that an intermediate value of $L'_{\text{CO}(3-2)}/L'_{\text{CO}(1-0)} = 0.8$ between submillimeter galaxies (SMGs) and QSOs was adopted in Banerji et al. (2017) and Fan et al. (2019). However, our results in Section 4.2 indicate that the bolometric luminosities of our sample are dominated by central AGN emission, favoring the line ratios typical of QSOs. The CO-to-H $_2$ conversion factor, α_{CO} , relates the CO(1–0) luminosity to the total molecular gas mass. For the Milky Way, we have $\alpha_{\text{CO}} \sim 4.6 M_\odot (\text{K km s}^{-1} \text{pc}^2)^{-1}$ (Bolatto et al. 2013). However, for starburst galaxies, α_{CO} is significantly lower, with a value of $0.8 M_\odot (\text{K km s}^{-1} \text{pc}^2)^{-1}$ (Carilli & Walter 2013). We adopted $\alpha_{\text{CO}} = 0.8 M_\odot (\text{K km s}^{-1} \text{pc}^2)^{-1}$ for our galaxies, given the starburst nature (Fan et al. 2019) and the high merger fraction (Fan et al. 2016a) of Hot DOGs. The logarithmic molecular gas mass $\log M_{\text{H}_2}(M_\odot)$ of our sample ranges from 9.55 to 11.59, with a median value of 10.56. Our estimations of molecular gas mass based on CO line observations is 0.56 dex higher than the values predicted by dust mass assuming a Milky Way dust-to-gas ratio of 0.01 in Fan et al. (2016b). The line luminosities and molecular gas mass of our sample are listed in Table 5.

4.2. Results of the SED Fitting and Dust Properties

The best-fit SEDs are shown in Figure 2. Thanks to high AGN obscuration, the host galaxies of our Hot DOGs sample are easily observable, and the stellar emission can be separated out so that we can estimate the physical properties of the host galaxies. We adopted the median of the posterior probability distribution of each parameter as the fiducial value, and the uncertainties are reported as the 68% confidence intervals around the fiducial values. The derived properties are listed in Table 6. Based on our UV–millimeter three-component SED

modeling described in Section 3, the stellar population parameters, including stellar masses and SFRs, as well as the cold dust properties from the cold dust component and AGN luminosities, have been obtained.

The cold dust IR luminosity L_{IR} was calculated by integrating the cold dust component from 8 to 1000 μm . Our Hot DOGs exhibit $L_{\text{IR}} \sim 10^{13} L_\odot$. The estimated dust temperatures range from 42 to 48 K, with a median of 45 K, consistent with $T_{\text{dust}}-L_{\text{IR}}$ relation of SMGs (e.g., Magnelli et al. 2012; Roseboom et al. 2012). The parameter β denotes the power-law index of the optical depth, with $\tau_\lambda = \left(\frac{\lambda_0}{\lambda}\right)^\beta$. It ranges from 2.0 to 2.8, with a median of 2.5. The measured T_{dust} and β of the Hot DOGs are similar to the most luminous quasar found at $z = 6.327$ (Tripodi et al. 2023). A relatively high β value indicates optically thick dust in IR bands, which has also been reported in other compact starburst galaxies (e.g., Scoville et al. 2017). With the cold dust temperature T_{dust} and the emissivity index β , we derived the dust mass with the formula:

$$M_{\text{dust}} = \frac{D_L^2}{(1+z)} \times \frac{S_{\nu_{\text{obs}}}}{\kappa_{\nu_{\text{rest}}} B(\nu_{\text{rest}}, T_{\text{dust}})}, \quad (2)$$

where D_L is the luminosity distance, $S_{\nu_{\text{obs}}}$ is the flux density at observed frequency ν_{obs} , $\kappa_{\nu_{\text{rest}}} = \kappa_0(\nu/\nu_0)^\beta$ is the absorption coefficient at the corresponding rest-frame frequency, and $B(\nu_{\text{rest}}, T_{\text{dust}})$ is the Planck function per unit frequency at temperature T_{dust} . We adopted $\kappa_{850\mu\text{m}} = 3.8 \text{ cm}^2 \text{ g}^{-1}$ following Wu et al. (2014) and Fan et al. (2016b, 2019). The estimated dust masses of our sample are consistent with previous IR SED decomposition results in Fan et al. (2016b), with a sample median of $8.0 \times 10^7 M_\odot$. We note that β was fixed to 1.6 in Fan et al. (2016b) to avoid degeneracy. The uncertainties in the dust masses shown in Table 6 would be larger if we consider the adopted $\kappa_{850\mu\text{m}}$ value, which can

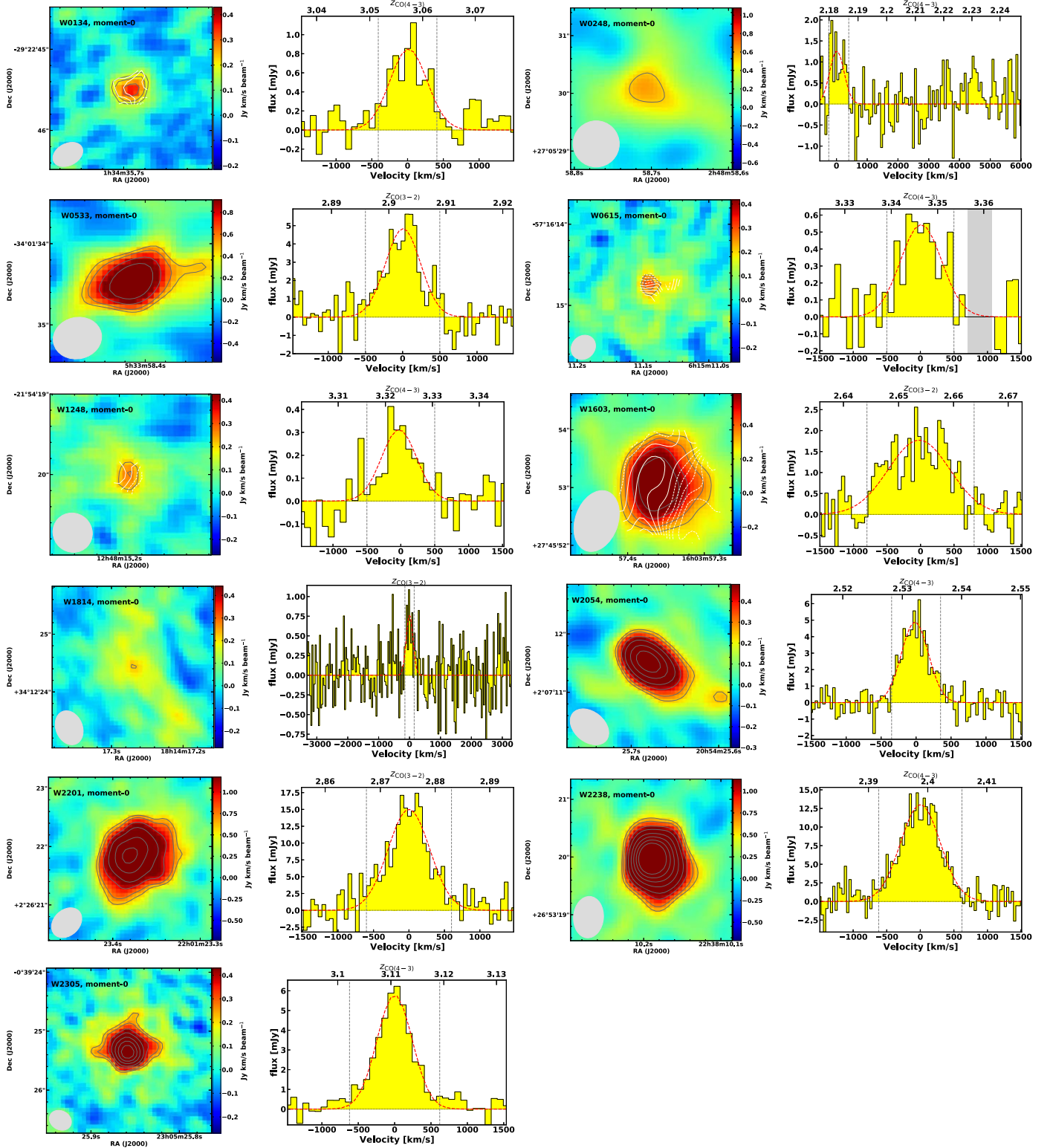


Figure 1. The CO emission line moment 0 maps and continuum-subtracted spectra.

vary from ~ 0.4 to $\sim 11 \text{ cm}^2 \text{ g}^{-1}$ (e.g., James et al. 2002; Draine 2003; Dunne et al. 2003; Siebenmorgen et al. 2014). All these dust properties are listed in Table 6.

Together with the CO measurements, these parameters allow us to derive the molecular gas fractions and SFEs (Table 7).

5. Discussion

5.1. Gas-to-dust Ratio

The estimated molecular gas mass M_{H_2} is plotted as a function of M_{dust} in Figure 3. The two dashed lines represent gas-to-dust ratios $\delta_{\text{GDR}} = 50$ and 150, which cover the typical

Table 5
CO Line Luminosities and Molecular Gas Masses

Source (1)	Redshift (2)	$L'_{\text{CO}(4-3)}$ (3)	$L'_{\text{CO}(3-2)}$ (4)	$L'_{\text{CO}(1-0)}$ (5)	M_{H_2} (6)
W0134-2922	3.057	1.48 ± 0.24	...	1.7 ± 0.28	1.36 ± 0.22
W0149+2350 ^a	3.23	2.40 ± 0.50	...	2.76 ± 0.57	2.21 ± 0.46
W0220+0137 ^a	3.136	3.39 ± 0.65	...	3.9 ± 0.75	3.12 ± 0.60
W0248+2705	2.183	1.12 ± 0.40	...	1.29 ± 0.46	1.03 ± 0.37
W0410-0913 ^a	3.63	17.90 ± 1.50	...	20.57 ± 1.72	16.46 ± 1.38
W0533-3401	2.902	...	12.50 ± 1.70	12.88 ± 1.75	10.30 ± 1.40
W0615-5716	3.346	1.30 ± 0.27	...	1.49 ± 0.31	1.19 ± 0.25
W1248-2154	3.323	0.62 ± 0.15	...	0.71 ± 0.18	0.57 ± 0.14
W1603+2745	2.654	...	7.65 ± 0.96	7.89 ± 0.99	6.31 ± 0.79
W1814+3412	2.457	0.38 ± 0.15	...	0.44 ± 0.17	0.35 ± 0.14
W2054+0207	2.532	4.63 ± 0.45	...	5.32 ± 0.52	4.26 ± 0.42
W2201+0226	2.875	...	47.4 ± 4.20	48.87 ± 4.33	39.10 ± 3.46
W2210-3507	2.814	...	<1.40	<1.44	<1.15
W2238+2653	2.399	17.20 ± 1.00	...	19.77 ± 1.15	15.82 ± 0.92
W2246-0526 ^b	4.601	8.98 ± 1.90	7.18 ± 1.52
W2305-0039	3.111	9.66 ± 0.59	...	11.10 ± 0.68	8.88 ± 0.54

Notes. Column (1): source name. Column (2): spectroscopic redshift. Columns (3) and (4): observed CO(4–3) and CO(3–2) line luminosity (units of $10^{10} \text{ K km s}^{-1} \text{ pc}^2$) calculated from the line flux I_{CO} in Table 4. Column (5) CO(1–0) line luminosity (units of $10^{10} \text{ K km s}^{-1} \text{ pc}^2$) adopting $L'_{\text{CO}(3-2)}/L'_{\text{CO}(1-0)} = 0.97$ and $L'_{\text{CO}(4-3)}/L'_{\text{CO}(1-0)} = 0.87$. Column (6) Molecular gas mass (units of $10^{10} M_{\odot}$) assuming $\alpha_{\text{CO}} \sim 0.8 M_{\odot} (\text{K km s}^{-1} \text{ pc}^2)^{-1}$.

^a From Fan et al. (2018).

^b From Díaz-Santos et al. (2018).

values derived for the Milky Way (Jenkins 2004), local star-forming galaxies (Draine et al. 2007; Rémy-Ruyer et al. 2014), and high-redshift SMGs (Magnelli et al. 2012; Miettinen et al. 2017). Most of our Hot DOGs exhibit a high δ_{GDR} value $\sim 474^{+711}_{-324}$, with a median uncertainty of 43% (uncertainties propagated from M_{H_2} and M_{dust}). Bischetti et al. (2021) found a median δ_{GDR} value of 180 for their nine hyperluminous, type I quasars at $z \sim 2-4$, slightly higher than typical values, and they attributed this to an increasing δ_{GDR} with redshift (e.g., Miettinen et al. 2017). We note that our sample is selected to have Herschel PACS and SPIRE observations, and have either SPIRE 500 μm or SCUBA-2 850 μm detection, and therefore may be biased toward the most intense starbursting systems, where supernova-shock-driven dust heating and destruction may be more significant (Jones 2004). The dust mass decreases with increasing dust temperature (Fan et al. 2016b, and references therein). The estimated $T_{\text{dust}} \sim 45 \text{ K}$ may trace a warmer dust component associated with photodissociation regions by starbursts, instead of the diffuse ISM with temperature below 30 K which represents the bulk of the dust mass (Draine & Li 2007; Liang et al. 2019; Sommovigo et al. 2020; Pozzi et al. 2021). The dust mass estimated from a simplistic graybody model may be underestimated by up to a factor of 3 compared to that derived by the dust models (for example, Draine & Li 2007), which include more parameters and adequately describe the multicomponent dust properties (Conroy 2013, and references therein). When we take a dust temperature of 30 K we find that the dust mass increases by ~ 0.5 dex and the corresponding δ_{GDR} approximately decreases by a factor of 3.

5.2. Stellar Mass and Molecular Gas Fraction

The logarithmic stellar masses range from 10.3 to 12.1, with a median of 10.8, indicating the majority of our Hot DOGs are massive galaxies. However, Díaz-Santos et al. (2021)

discovered higher SED-based stellar masses than dynamical masses based on ALMA [C II] observations. They attributed this overestimation to the lower angular resolution of optical/NIR data than that of interferometric [C II] data. We defer a comparative analysis of the stellar and dynamical masses of our sample to a future work. With M_* derived from SED fitting and molecular gas mass M_{H_2} inferred from CO line observations, we calculated the molecular gas fraction, which is defined as $f_{\text{gas}} = M_{\text{H}_2}/(M_{\text{H}_2} + M_*)$, and listed the results in Table 7. Due to the lack of optical–NIR photometry data for W0248+2705, W0615-5716, and W1248-2154, we cannot obtain SED-based stellar masses M_* for these three Hot DOGs. To put an upper limit on the molecular gas fraction for these three Hot DOGs, we adopted $M_* = 10^{10.3} M_{\odot}$, which is the minimum M_* estimated for the other galaxies in our sample.

Our Hot DOGs have comparable redshift and stellar mass ranges to the SMGs studied in Miettinen et al. (2017; $z \sim 2.3$ and $\log M_* (M_{\odot}) = 11.09^{+0.41}_{-0.53}$, respectively). However, the molecular gas fraction of our Hot DOGs ($0.33^{+0.33}_{-0.17}$) is much lower than the SMGs in Miettinen et al. (2017; $0.62^{+0.27}_{-0.23}$).

In Figure 4, we show the molecular gas fraction f_{gas} as a function of redshift for our Hot DOGs, as well as literature samples of SMGs, obscured quasars at $z > 1$ from Perna et al. (2018), and Palomar–Green (PG) quasars in the local Universe from Shanguan et al. (2020). We note that the median uncertainty of f_{gas} of our Hot DOG sample is approximately 60%, which results from the uncertainties in M_{H_2} and M_* and is shown as gray in the bottom-right corner in Figure 4. The sample of high-redshift SMGs from Miettinen et al. (2017) is also represented in this figure. These literature samples all have $M_* \sim 10^{11} M_{\odot}$, which is comparable to our Hot DOGs. To demonstrate how the molecular gas fractions of these galaxies compare with main-sequence (MS) galaxies, we present the gas fraction evolutionary trends for MS galaxies of mass $M_* = 10^{11} M_{\odot}$, $M_* = 2 \times 10^{10} M_{\odot}$, and $M_* = 5 \times 10^{11} M_{\odot}$ predicted from the 2-SFM model (Sargent et al. 2014). It is

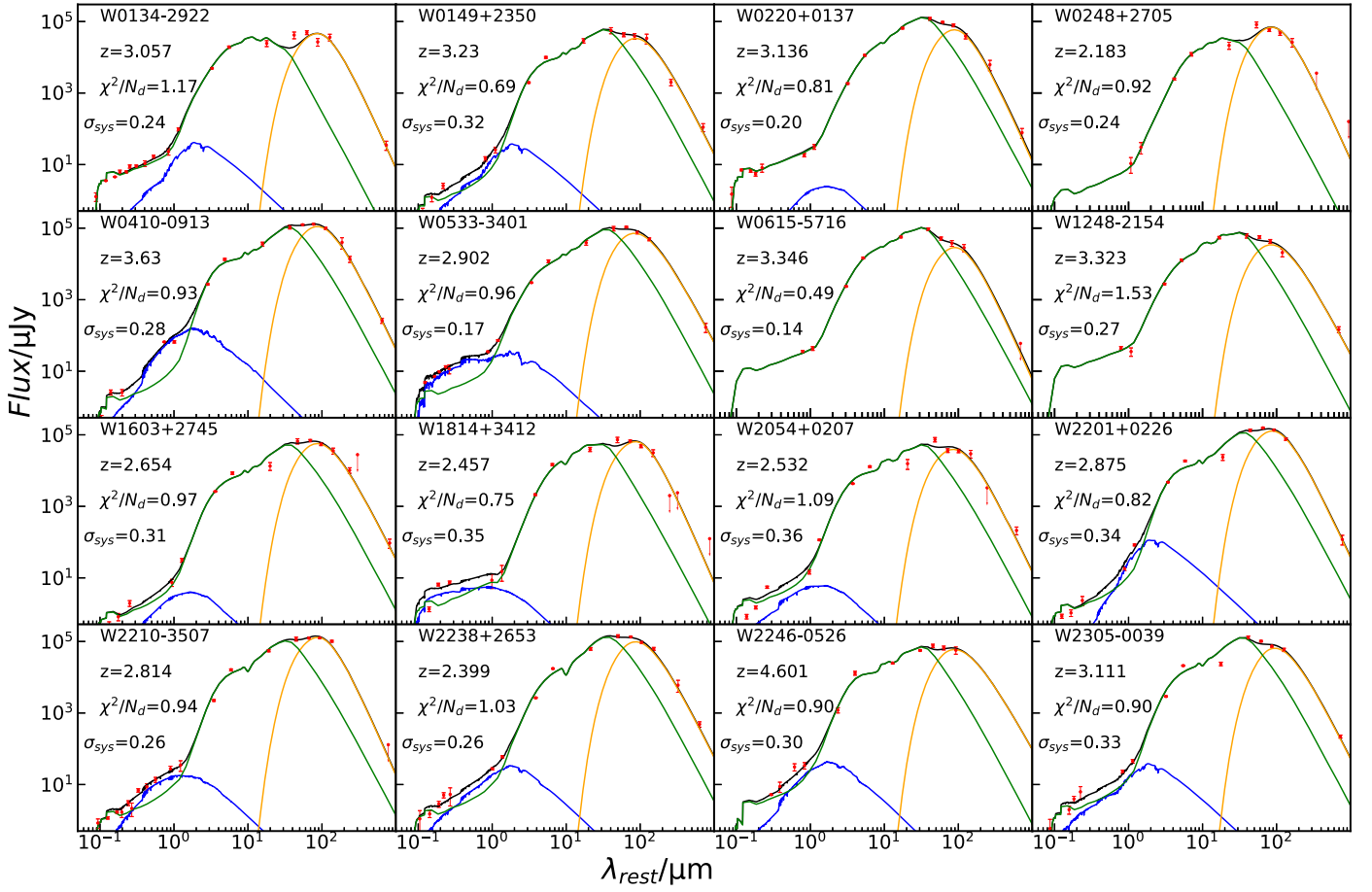


Figure 2. Best-fit model SEDs by T_{dust} -constrained fitting for 16 Hot DOGs in our sample. The source ID, redshift, χ^2/N_d (N_d is the number of photometric data points), and the systematical errors (see Han & Han 2014) are shown in each panel. The red points with error bars represent the observed photometric data, and those with downward arrows mark flux density upper limits. The solid blue, orange, and green lines represent, respectively, the stellar, cold dust, and AGN components. The solid black line represents the total SED.

worth noting that a significant proportion of the SMGs compiled in Perna et al. (2018) exhibit AGN activity, while the SMG sample in Miettinen et al. (2017) has excluded SMGs that demonstrate evidence of hosting an AGN. Similar to the PG QSOs from Shangguan et al. (2020) and the SMGs and obscured QSOs from Perna et al. (2018), the f_{gas} of most of our Hot DOGs is below the relation for MS galaxies with comparable M_* . This is consistent with the results of Díaz-Santos et al. (2018) and Penney et al. (2020), who concluded that Hot DOGs may have a lower cold molecular gas content than ordinary star-forming galaxies. The sample of SMGs lacking AGN exhibits a higher molecular gas fraction compared to MS galaxies. The discrepancy in f_{gas} between active and normal galaxies is likely due to the depletion of cold gas by AGN feedback. We color coded our Hot DOGs in the figure according to their AGN bolometric luminosity L_{AGN} , derived by integrating the AGN component of the best-fit UV to millimeter SED. Most Hot DOGs with an f_{gas} lower than MS galaxies exhibit a relatively higher L_{AGN} , which is consistent with recent findings of a positive correlation between the efficiency of AGN feedback traced by the mass outflow rate and L_{AGN} (see, e.g., Hopkins et al. 2016; Fiore et al. 2017; García-Burillo et al. 2021). AGN-driven outflows deposit energy and momentum into the surrounding gas and affect the evolution of the host galaxy by heating and ejecting the ISM (e.g., Weymann et al. 1991; Faucher-Giguère & Quataert 2012;

Marasco et al. 2020). Our Hot DOGs stand out from the other samples by their extremely high L_{AGN} , which may explain their relatively large deviation from the MS relation.

5.3. Star Formation Rate and Star Formation Efficiency

The SFRs of Hot DOGs were derived by averaging the modeled exponential SFH in the last 100 Myr. The cold dust component is modeled by adding a graybody component, whose energy budget is identical to the attenuated luminosity in the UV–optical band, i.e., the so-called energy balance assumption. Figure 5 shows that our sample generally follows the relation of SFR ($M_{\odot} \text{ yr}^{-1}$) = $8 \times 10^{-11} L_{\text{IR}} (L_{\odot})$, which is about 0.1 dex lower than the Kennicutt (1998) relation calibrated by the Chabrier (2003) IMF. For the three sources without an optical–NIR detection, we estimate their SFRs based on the relation between SFR and L_{IR} calibrated for the remaining 13 Hot DOGs. The SFRs estimated for our Hot DOGs are shown in Table 6. By invoking the MS evolutionary model of Speagle et al. (2014):

$$\log(\text{SFR}/M_{\odot} \text{ yr}^{-1}) = (0.84 - 0.026 \times \tau_{\text{univ}}) \log(M_*/M_{\odot}) - (6.51 - 0.11 \times \tau_{\text{univ}}), \quad (3)$$

where τ_{univ} is the age of the Universe in gigayears, we can estimate the offset of our Hot DOGs from the MS $\Delta_{\text{MS}} = \text{SFR}/\text{SFR}_{\text{MS}}$ relation. The high Δ_{MS} values (Table 7) demonstrate that most of our Hot DOGs are extreme starburst

Table 6
Summary of the Results of the SED Fitting

Source	T_{dust} (K)	$T_{\text{dust},0}$ (K)	β	$\log(L_{\text{AGN}})$ $\log(L_{\odot})$	$\log(L_{\text{IR}})$ $\log(L_{\odot})$	$\log(L_{\text{IR},0})$ $\log(L_{\odot})$	$\log(M_{\text{dust}})$ $\log(M_{\odot})$	$\log(\text{SFR})$ $\log(M_{\odot} \text{ yr}^{-1})$	$\log(M_{*})$ $\log(M_{\odot})$	δ_{GDR}
(1)	(2)	(3)	(4)	(5)	(6)	(7)	(8)	(9)	(10)	(11)
W0134–2922 ^b	48.03 ^{+1.33} _{-2.34}	72.73 ^{+9.75} _{-9.68}	2.78 ^{+0.12} _{-0.16}	13.98 ^{+0.02} _{-0.02}	12.97 ^{+0.01} _{-0.02}	13.18 ^{+0.06} _{-0.07}	7.40 ^{+0.15} _{-0.10}	2.91 ^{+0.13} _{-0.16}	10.61 ^{+0.45} _{-0.35}	453 ⁺¹⁰¹ ₋₁₈₇
W0149+2350	44.64 ^{+2.29} _{-4.56}	84.04 ^{+9.40} _{-14.72}	2.42 ^{+0.23} _{-0.23}	13.92 ^{+0.02} _{-0.03}	12.92 ^{+0.05} _{-0.05}	13.31 ^{+0.07} _{-0.13}	7.81 ^{+0.18} _{-0.17}	2.77 ^{+0.17} _{-0.21}	10.82 ^{+0.35} _{-0.41}	339 ⁺¹³³ ₋₁₉₆
W0220+0137 ^b	45.33 ^{+2.97} _{-3.78}	63.58 ^{+12.60} _{-11.39}	2.72 ^{+0.15} _{-0.16}	14.15 ^{+0.02} _{-0.02}	13.09 ^{+0.05} _{-0.05}	13.31 ^{+0.13} _{-0.13}	7.68 ^{+0.14} _{-0.12}	3.06 ^{+0.11} _{-0.15}	10.55 ^{+0.38} _{-0.23}	638 ⁺²⁰² ₋₂₈₆
W0248+2705 ^a	47.44 ^{+1.76} _{-3.50}	69.16 ^{+6.67} _{-7.67}	2.47 ^{+0.33} _{-0.40}	13.51 ^{+0.02} _{-0.02}	12.89 ^{+0.02} _{-0.05}	13.12 ^{+0.05} _{-0.06}	7.61 ^{+0.34} _{-0.26}	2.78 ^{+0.02} _{-0.05}	...	250 ⁺¹⁴⁵ ₋₃₁₄
W0410–0913	47.35 ^{+1.78} _{-2.57}	74.62 ^{+8.30} _{-8.83}	2.63 ^{+0.16} _{-0.18}	14.21 ^{+0.04} _{-0.03}	13.51 ^{+0.03} _{-0.03}	13.80 ^{+0.05} _{-0.08}	8.09 ^{+0.14} _{-0.12}	3.08 ^{+0.13} _{-0.04}	12.08 ^{+0.10} _{-0.25}	1325 ⁺³⁴⁶ ₋₅₄₉
W0533–3401	46.52 ^{+2.37} _{-4.07}	79.21 ^{+7.05} _{-8.45}	2.26 ^{+0.21} _{-0.19}	13.98 ^{+0.02} _{-0.02}	13.14 ^{+0.04} _{-0.06}	13.55 ^{+0.05} _{-0.07}	8.08 ^{+0.14} _{-0.16}	3.16 ^{+0.12} _{-0.17}	10.65 ^{+0.34} _{-0.23}	845 ⁺²⁹⁷ ₋₃₆₉
W0615–5716 ^a	45.34 ^{+3.11} _{-3.88}	73.38 ^{+15.42} _{-17.19}	2.75 ^{+0.15} _{-0.18}	14.21 ^{+0.01} _{-0.01}	12.83 ^{+0.05} _{-0.04}	13.14 ^{+0.15} _{-0.20}	7.43 ^{+0.15} _{-0.16}	2.72 ^{+0.05} _{-0.04}	...	440 ⁺¹⁶⁸ ₋₂₁₅
W1248–2154 ^a	45.37 ^{+3.15} _{-5.02}	74.59 ^{+11.83} _{-12.23}	2.13 ^{+0.21} _{-0.19}	14.14 ^{+0.03} _{-0.03}	12.91 ^{+0.05} _{-0.07}	13.22 ^{+0.09} _{-0.11}	8.00 ^{+0.16} _{-0.15}	2.80 ^{+0.05} _{-0.07}	...	56 ⁺²¹ ₋₂₉
W1603+2745 ^b	44.87 ^{+3.32} _{-5.02}	67.00 ^{+7.02} _{-7.66}	2.35 ^{+0.21} _{-0.20}	13.65 ^{+0.03} _{-0.03}	12.98 ^{+0.06} _{-0.08}	13.26 ^{+0.05} _{-0.06}	7.91 ^{+0.16} _{-0.15}	2.91 ^{+0.14} _{-0.19}	10.58 ^{+0.46} _{-0.31}	762 ⁺²⁴⁷ ₋₃₅₉
W1814+3412	46.59 ^{+2.32} _{-3.61}	73.43 ^{+10.89} _{-11.05}	2.75 ^{+0.16} _{-0.24}	13.73 ^{+0.02} _{-0.02}	12.93 ^{+0.03} _{-0.05}	13.20 ^{+0.08} _{-0.09}	7.45 ^{+0.23} _{-0.16}	2.92 ^{+0.10} _{-0.13}	10.34 ^{+0.31} _{-0.19}	122 ⁺⁶⁰ ₋₉₈
W2054+0207 ^b	41.98 ^{+5.23} _{-5.84}	79.23 ^{+8.39} _{-8.57}	2.53 ^{+0.25} _{-0.27}	13.72 ^{+0.03} _{-0.03}	12.71 ^{+0.09} _{-0.09}	13.18 ^{+0.06} _{-0.07}	7.64 ^{+0.21} _{-0.19}	2.59 ^{+0.19} _{-0.24}	10.54 ^{+0.52} _{-0.46}	974 ⁺³⁶⁶ ₋₆₄₂
W2201+0226	45.85 ^{+2.75} _{-3.79}	72.06 ^{+5.56} _{-6.73}	2.70 ^{+0.16} _{-0.23}	14.03 ^{+0.03} _{-0.03}	13.39 ^{+0.05} _{-0.05}	13.60 ^{+0.03} _{-0.05}	8.00 ^{+0.19} _{-0.16}	3.26 ^{+0.18} _{-0.23}	11.24 ^{+0.39} _{-0.37}	3886 ⁺¹²⁷⁸ ₋₂₂₁₇
W2210–3507	45.32 ^{+2.84} _{-3.88}	60.33 ^{+9.25} _{-9.12}	2.78 ^{+0.13} _{-0.19}	13.98 ^{+0.02} _{-0.02}	13.35 ^{+0.03} _{-0.04}	13.52 ^{+0.07} _{-0.09}	7.92 ^{+0.17} _{-0.14}	3.23 ^{+0.17} _{-0.18}	11.14 ^{+0.38} _{-0.38}	162 ⁺⁵³ ₋₈₄
W2238+2653	44.76 ^{+3.59} _{-5.48}	72.92 ^{+9.28} _{-8.90}	2.41 ^{+0.22} _{-0.19}	13.90 ^{+0.02} _{-0.02}	13.15 ^{+0.06} _{-0.08}	13.50 ^{+0.07} _{-0.08}	8.04 ^{+0.14} _{-0.14}	3.07 ^{+0.16} _{-0.20}	10.76 ^{+0.47} _{-0.31}	1433 ⁺⁴²² ₋₅₈₆
W2246–0526	44.31 ^{+3.58} _{-3.24}	91.56 ^{+8.64} _{-12.21}	1.96 ^{+0.56} _{-0.56}	14.33 ^{+0.03} _{-0.04}	13.41 ^{+0.05} _{-0.05}	13.78 ^{+0.03} _{-0.08}	8.70 ^{+0.52} _{-0.53}	3.24 ^{+0.20} _{-0.22}	11.40 ^{+0.34} _{-0.30}	141 ⁺¹⁰⁴ ₋₁₃₀
W2305–0039	42.75 ^{+4.66} _{-6.28}	78.73 ^{+7.18} _{-10.15}	2.28 ^{+0.23} _{-0.22}	14.14 ^{+0.02} _{-0.02}	13.17 ^{+0.07} _{-0.09}	13.63 ^{+0.05} _{-0.08}	8.25 ^{+0.18} _{-0.14}	3.06 ^{+0.17} _{-0.20}	10.89 ^{+0.46} _{-0.39}	494 ⁺¹⁴² ₋₂₅₉

Notes. Median and 16th–84th quartile ranges of the parameter posterior probability distribution. Column (1): source name. Column (2): cold dust temperature. Column (3): cold dust temperature, but for the T_{dust} -unconstrained fitting. Column (4): dust emissivity index in the graybody function. Column (5): AGN bolometric luminosity by integrating the AGN component SED. Column (6): host galaxy IR luminosity by integrating the cold dust component SED. Column (7): host galaxy IR luminosity, but for the T_{dust} -unconstrained fitting. Column (8): dust mass. Column (9): SFR. Column (10): stellar mass. For the blue excess Hot DOGs (BHDs), their stellar mass may have larger uncertainties. Column (11): gas-to-dust ratio.

^a Sources without UV–optical data.

^b Sources identified as BHDs, as discussed in Section 5.5.

systems, which could be triggered by gas-rich galaxy mergers (e.g., Noguchi & Ishibashi 1986; Mihos & Hernquist 1996). With the molecular gas masses and SFRs, we derived the gas depletion timescale $t_{\text{depl}} = M_{\text{H}_2}/\text{SFR}$. Similar to obscured quasars (e.g., Aravena et al. 2008; Brusa et al. 2018), our Hot DOGs exhibit a short gas depletion timescale. In contrast, typical starburst galaxies have a t_{depl} value of several hundred megayears (e.g., Genzel et al. 2010; Bothwell et al. 2013; Miettinen et al. 2017). Hot DOGs have been discovered to exhibit outflow mass loss rates of several thousand solar masses per year (Finnerty et al. 2020). Considering these powerful AGN outflows, the gas depletion timescale could be shorter. The molecular gas in Hot DOGs may be depleted within several tens of megayears, resulting in the lower molecular gas fraction in Hot DOGs. The few Hot DOGs with a high gas fraction may represent a relatively earlier stage after AGN activity has been triggered.

In Figure 6, we show the SFEs ($=\text{SFR}/M_{\text{H}_2}$) as a function of IR luminosity L_{IR} for our Hot DOGs, as well as for the compiled samples of SMGs and unobscured and obscured quasars from Perna et al. (2018). We use the corresponding observables, L_{IR} obtained from the cold dust component of our SED decomposition and $L'_{\text{CO}(1-0)}$ acquired through ALMA observations, to calculate the SFE as $L_{\text{IR}}/L'_{\text{CO}(1-0)}$. The SFEs exhibit a tight correlation with L_{IR} for both MS galaxies (Sargent et al. 2014) and SMGs. Our Hot DOGs, along with obscured and unobscured quasars at $z > 1$, display high SFEs that are well above the relation for MS galaxies. This is likely due to the rapid depletion of cold gas by AGN feedback and star formation. We plot the relation between SFE and L_{AGN} for

the Hot DOGs and obscured quasars in Figure 7. We also included WISE- and SDSS-selected hyperluminous (WISSH) quasars from Bischetti et al. (2021) and PG QSOs from Shanguan et al. (2020). The AGN bolometric luminosities of the obscured quasars from Perna et al. (2018) are calculated from their X-ray luminosities, assuming a luminosity-dependent bolometric correction from Duras et al. (2020). Across all four quasar samples, there is a positive correlation between SFE and L_{AGN} . The Spearman’s rank correlation coefficient $\rho = 0.532$ ($p = 3.55 \times 10^{-8}$), where p is the probability of the null hypothesis that a correlation does not exist. When excluding the PG QSOs given that they are in local Universe, ρ decreases to 0.404 with $p = 2.21 \times 10^{-3}$. This correlation can be explained by the enhanced outflow rates in galaxies with a high AGN luminosity, and is consistent with their low gas fractions (Figure 4).

5.4. Influence of Active Galactic Nucleus Contamination on Far-infrared Luminosity

Initially, we fitted our sample with BayeSED by setting the T_{dust} parameter range to default values (10–100 K). However, we obtained dust temperatures ~ 60 –90 K, which are higher than found for DOGs and SMGs, but are consistent with previous studies employing a similar fitting methodology (Wu et al. 2012; Fan et al. 2016b, 2019). We refer to this SED fitting as T_{dust} -unconstrained fitting and denote the resulting dust temperature and cold dust luminosity as $T_{\text{dust},0}$ and $L_{\text{IR},0}$, respectively, which are listed in Table 6. The $L_{\text{IR},0}$ values are consistent with those given in Table 1. For the T_{dust} -unconstrained fitting, the FIR emission is entirely attributed to cold dust heated by massive stars.

Table 7
Summary of the Physical Properties

Statistics Value	δ_{GDR}	f_{gas}	Δ_{MS}	t_{depl} (Myr)	SFE (K km s ⁻¹ pc ⁻²)	M_{BH} (10 ⁹ M_{\odot})	M_{BH}/M_{\star}	\dot{M}_{BH} $M_{\odot} \text{ yr}^{-1}$
(1)	(2)	(3)	(4)	(5)	(6)	(7)	(8)	(9)
max	3886	0.73	15	222	1958	6.6	0.122	147
median, scatter	474^{+711}_{-324}	$0.33^{+0.33}_{-0.17}$	$6.12^{+5.1}_{-2.9}$	39^{+85}_{-28}	297^{+659}_{-195}	$3.0^{+1.8}_{-1.3}$	$0.042^{+0.029}_{-0.021}$	65^{+39}_{-29}
min	56	0.09	0.62	4	51	1.0	0.004	22

Notes. Column (1): sample maximum, median, and 16th–84th quartile range and minimum. Column (2): gas-to-dust ratio. Column (3): molecular gas fraction. Column (4): SFR offset against main-sequence (MS) galaxies. Column (5): gas depletion timescale. Column (6): SFE. Column (7): central black hole mass assuming $\lambda_{\text{Edd}} = 1.0$. Column (8): black hole to stellar mass ratio. Column (9): black hole growth rate.

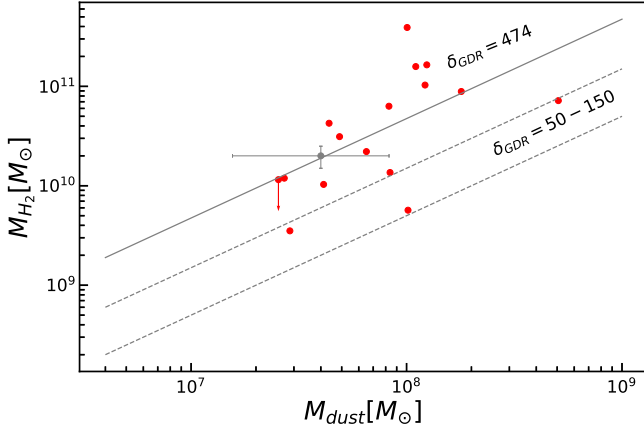


Figure 3. Molecular gas mass M_{H_2} vs. cold dust mass M_{dust} . The red points represent our sample values, while the downward arrows mark the upper limit molecular gas mass for W2210–3507. The typical uncertainties are shown as a gray point with error bars. The two dashed lines represent a gas-to-dust ratio δ_{GDR} value of 50–150, which is the typical value derived for the Milky Way (Jenkins 2004), local star-forming galaxies (Draine et al. 2007; Rémy-Ruyer et al. 2014), and high-redshift SMGs (Magnelli et al. 2012; Miettinen et al. 2017). The solid line represents a gas-to-dust ratio δ_{GDR} value of 521, which is typical for our sample based on the SED analysis and ALMA observations.

However, many studies suggested that AGNs could heat dust up to kiloparsec scales, significantly contributing to their FIR emission (see Section 7 in Netzer 2015 for a recent review). For example, Schneider et al. (2015) conducted radiative transfer modeling and reported that AGN-heated dust contributes from 30% up to 70% of the FIR luminosity for a high-redshift quasar host galaxy. Duras et al. (2017) employed the same technique and found a 40% to 60% quasar contribution to the FIR emission for their sample. Tsukui et al. (2023) determined an AGN contribution of approximately 53% based on image decomposition of spatially resolved ALMA continuum observations. The high cold dust temperature estimated for Hot DOGs may result from a contribution by AGN-heated warmer dust, similar to the findings of Tsukui et al. (2023).

The hot dust MIR emission from the central torus may be reprocessed to the FIR by optical thick dust in nuclear region (e.g., Scoville et al. 2017; Sokol et al. 2023). Additionally, the FIR contribution of the central AGN may also originate from emission by narrow-line region (NLR) polar dust, which has been proven to be heterogeneous in nearby AGNs (Netzer 2015, and references therein). Given the high AGN luminosities of our Hot DOGs, the NLR dust is expected to extend to kiloparsec scales. González-Martín et al. (2019) improved SED fitting for higher-luminosity AGN by employing the two-

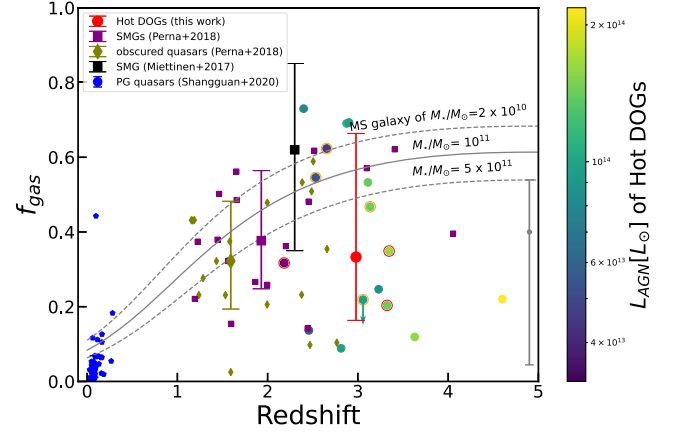


Figure 4. Molecular gas fraction f_{gas} as a function of redshift. The 16 Hot DOGs represented by circle symbols in our sample are color coded according to their AGN bolometric luminosity, and their typical uncertainties are plotted in the bottom-right corner as a gray point with error bars. The three sources that did not have an SED-based stellar mass and were estimated to have a stellar mass of $10^{10.3} M_{\odot}$ are additionally highlighted with red circles, and four sources whose optical emission are dominated by an AGN component (Section 5.4) are additionally highlighted with orange circles. The purple square and olive diamond symbols represent the samples of SMGs and obscured quasars, respectively, compiled in Perna et al. (2018). The black squares represent the sample of SMGs in Miettinen et al. (2017). Note that Miettinen et al. (2017) have excluded from their sample SMGs with evidence of an AGN, whereas a large fraction of SMGs studied by Perna et al. (2018) have AGN activities. The blue pentagon represents the sample of local PG quasars in Shanguan et al. (2020). The median and 16th–84th quartile range of our Hot DOGs are shown as a larger filled red circle with error bars, and the sample median and 16th–84th quartile range of the literature samples are shown correspondingly with larger symbols with error bars. The redshift evolutionary trend predicted from the 2-SFM model (Sargent et al. 2014) of MS galaxies of $M_{\star} = 10^{11} M_{\odot}$ (typical for our sample) is shown as a solid curve, while MS galaxies of $M_{\star} = 2 \times 10^{10} M_{\odot}$ and $M_{\star} = 5 \times 10^{11} M_{\odot}$ are labeled with dashed lines.

component models proposed by Hönig & Kishimoto (2017), which incorporate a clumpy disk and a polar clumpy wind, in contrast to the CLUMPY model. There is evidence suggesting that the extended polar dust emission is likely associated with AGN-driven dusty outflows (e.g., Alonso-Herrero et al. 2021). Lyu & Rieke (2018) utilized their AGN SED libraries, which include an extended polar dust component, to model the SEDs of Hot DOGs. Their results attribute a significant portion of the FIR emission to the polar dust component.

It is crucial to consider accurately the AGN contribution to the FIR emission and to estimate the cold dust luminosity appropriately. Based on the flux density ratios of 350 μm and 1.1 mm continuum of several Hot DOGs, Wu et al. (2012, 2014) suggested that the cold dust component heated by star formation is not very different from those in starburst galaxies,

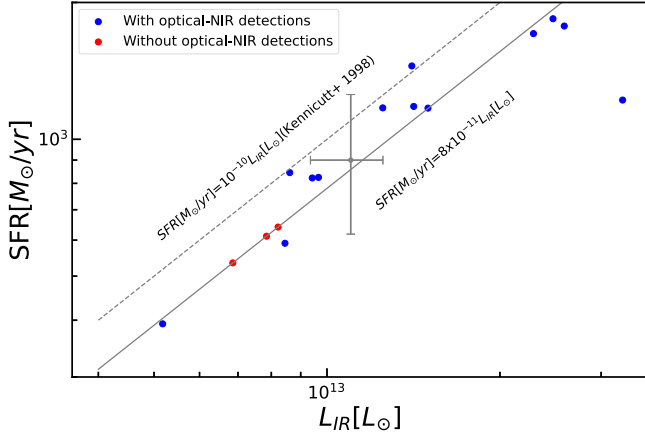


Figure 5. SFR traced by IR luminosity. The sources with optical–NIR detections are shown as blue circles, and they can be represented by the relation labeled with a solid curve in the figure, which is about 0.10 dex lower than the Kennicutt (1998) relation calibrated by the Chabrier IMF. The SFRs of three Hot DOGs without optical–NIR photometry, namely W0248+2705, W0615–5716, and W1248–2154, are calculated based on this relation. Their typical uncertainties are shown as a gray point with error bars.

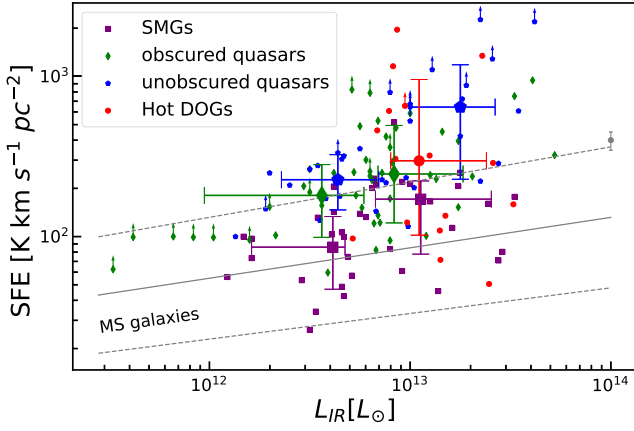


Figure 6. SFE traced by the ratio of IR to CO(1–0) line luminosity as a function of IR luminosity L_{IR} . Our sample is labeled with red circles. The typical uncertainties are shown as a gray point with error bars. The purple squares, olive diamonds, and blue pentagons represent the samples of SMGs, obscured quasars, and unobscured quasars, respectively, compiled in Perna et al. (2018). The upward arrows mark lower limits. Each sample in Perna et al. (2018) has been divided into two bins according to IR luminosity. The median values of the galaxies in the various samples mentioned above are shown with larger symbols, overlaid by their 16th–84th quantile ranges as error bars. The solid line shows the best-fit relation for massive MS galaxies, and the 1σ scatter is indicated with two dashed lines (Sargent et al. 2014).

characterized by temperatures ranging between 30 and 50 K (e.g., Magnelli et al. 2012). We constrained the T_{dust} parameter of the graybody component to be within the range 30–50 K and refitted the SEDs in our sample. This fitting approach is denoted as T_{dust} -constrained fitting. We show an example in Figure 8, which compares the best-fit SEDs obtained via T_{dust} -constrained fitting (solid line) and T_{dust} -unconstrained fitting (dash line). For the T_{dust} -constrained fitting, the AGN emission dominates up to rest-frame 50 μm , while for the T_{dust} -unconstrained fitting, the AGN emission only dominates up to rest-frame 25 μm . The reduced χ^2 only improve by a value of 0.10 after we apply our prior knowledge of T_{dust} for W0533–3401. We calculate the Bayes factor, defined as the difference in the Bayesian evidence

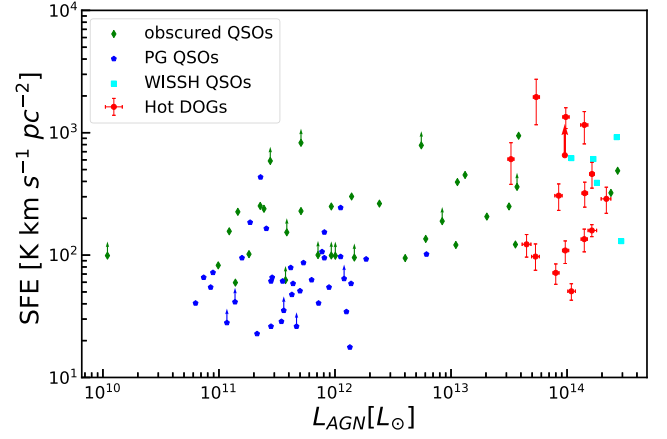


Figure 7. Positive correlation between SFE and AGN bolometric luminosity. Red circles with error bars represent our Hot DOGs. Green diamond symbols represent the sample of obscured quasars in Perna et al. (2018). The blue pentagons represent the sample of local PG quasars in Shanguan et al. (2020). Cyan square symbols represent the sample of hyperluminous, type I quasars at $z \sim 1$ –4 in Bischetti et al. (2021). The downward arrows mark upper limits.

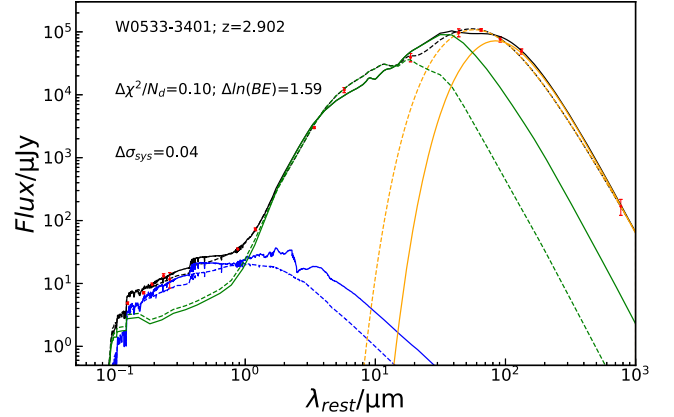


Figure 8. Best-fit model SED comparison between T_{dust} -constrained fitting (solid line) and T_{dust} -unconstrained fitting (dashed line) for W0533–3401. The source ID, redshift, χ^2/N_d offset, Bayes factor offset, and the systematical error offset (see Han & Han 2014) are shown on the panel. The color of the legend is identical to that of Figure 2.

between the two fitting methods, to be in the range 0.1–3.6, suggesting no strong evidence in favor of the T_{dust} -unconstrained fitting (Han & Han 2014). In the earliest torus model, Pier & Krolik (1993) enlarged the torus to account for the FIR emission by a ~ 100 pc scale torus. Similarly, for the CLUMPY model of Nenkova et al. (2008a, 2008b), the AGN FIR emission can come from an extended torus with a large torus outer radius $R_{\text{out}} = Y R_{\text{in}}$ (Drouart et al. 2014), where Y is the radial extent, one of the six free parameters used to define the CLUMPY model. R_{in} is the inner radius set by the location of the dust at the sublimation temperature, and is computed using the AGN bolometric luminosity L_{AGN} by the equation:

$$R_{\text{in}} = 0.4 \left(\frac{L_{\text{AGN}}}{10^{45} \text{ erg s}^{-1}} \right)^{0.5} \text{ pc}. \quad (4)$$

Based on the T_{dust} -constrained fitting, we obtain $L_{\text{AGN}} \sim 10^{47.6} L_{\odot}$ and $Y \sim 65$ for our sample, which give $R_{\text{out}} \sim 0.5$ kpc. L_{IR} is

smaller by 0.16–0.47 dex compared to the $L_{\text{IR},0}$ shown in Table 6, as a significant proportion of the FIR emission is assigned to the AGN component modeled by CLUMPY model. This is generally consistent with the results of Díaz-Santos et al. (2021). Based on the ALMA dust continuum image measurements, they observed that Hot DOGs do not exhibit a particularly small FIR size, and the unresolved central AGN component contributes to some extent (from 20% up to 80% in the most extreme cases) but does not dominate the FIR emission. Overall, we believe that the T_{dust} -constrained fitting method effectively considers the AGN contribution to the FIR. The analysis of the physical properties in this paper is entirely based on the T_{dust} -constrained fitting.

5.5. The Applicability of the CLUMPY Model to Hot DOGs with Excess Blue Light

Hot DOGs are usually under heavy dust obscuration, and optically seen as type 2 AGN (Wu et al. 2012). However, Assef et al. (2016) discovered a subpopulation of eight Hot DOGs which exhibit a blue UV–optical SED similar to the blue bump caused by the AGN accretion disk. They named them BHDs. Their rest-frame UV spectra are of typical type 1 quasars, showing broad emission lines (Assef et al. 2020). They confirmed that the UV–optical SEDs of this subpopulation of Hot DOGs are due to 1% scattered light from the highly obscured, hyperluminous AGN into our line of sight, using X-ray and imaging polarization observations (Assef et al. 2016, 2020, 2022). One Hot DOG in our sample, namely W0220+0137, has been identified as a BHD in Assef et al. (2016, 2020).

The CLUMPY model of Nenkova et al. (2008a, 2008b) is a geometrical torus model that assumes a certain geometry and dust composition when conducting radiative transfer modeling. The absorption and scattering coefficients given in Ossenkopf et al. (1992) are used, where the UV–optical emission is dominated by AGN-scattered radiation (Nenkova et al. 2008a). Ichikawa et al. (2015) employed the CLUMPY model to fit the SEDs of type 2 Seyferts with scattered light or a hidden broad-line region (HBLR), which is similar to BHDs, and they identified differences in the modeled torus geometry of HBLRs compared to type 2 Seyferts lacking HBLR signatures. As shown in Figure 2, our SED modeling of W0220+0137 is consistent with the results of Assef et al. (2016, 2020), where the UV–optical SED is dominated by an AGN component. For almost all other Hot DOGs with an optical detection, we found that the UV light is dominated by AGN component. There are three Hot DOGs, namely W0134–2922, W1603+2745, and W2054+0207, whose optical–NIR band also exhibits more AGN emission than stellar emission. These objects are also likely to be compatible with BHDs, albeit to a relatively less extent. For these four BHDs, their stellar mass estimations are more uncertain. For example, Merloni et al. (2010) decomposed the UV to MIR SEDs of 89 type 1 AGNs with two-component SED fitting, and they assigned an upper limit to the stellar mass for galaxies whose contribution of stellar light in the K band is less than 5%. None of our Hot DOGs exhibit such a low stellar contribution, and the cold dust FIR emission from the host galaxy serves as an additional constraint on the stellar component. We have highlighted these four galaxies in Table 6 and Figure 4. We also note that W2246–0526 and W2305–0039 have nearly equal contributions from AGN and stellar components in the optical–NIR band.

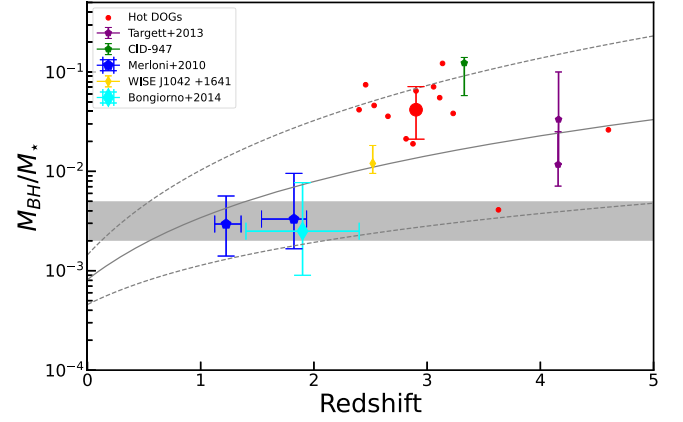


Figure 9. Redshift evolution of the black hole to stellar mass ratio (M_{BH}/M_*). The M_{BH}/M_* ratios of Hot DOGs are shown as red circles, and the sample median and 16th–84th quantile ranges are shown as a larger symbol with error bars. Blue triangles represent a sample of 89 moderately luminous broad-line AGN in the redshift range $1 < z < 2.2$ (Merloni et al. 2010). A sample of 21 X-ray obscured, red AGNs with moderate luminosity in Bongiorno et al. (2014) is labeled with cyan diamond symbols. For luminous quasars with AGN bolometric luminosity $> 10^{46} \text{ erg s}^{-1}$, two luminous SDSS quasars at $z \sim 4$ (Targett et al. 2012) and an extremely red dust-obscured quasar (Toba & Nagao 2016; Matsuoka et al. 2018) are denoted with purple filled triangles and a gold filled square, respectively. The green-filled diamond denotes an X-ray-selected luminous unobscured quasar, CID-947, at $z \sim 3.3$, which has an extremely high black hole to stellar mass ratio $M_{\text{BH}}/M_* = 1/8$ (Trakhtenbrot et al. 2015). The solid line and two dashed lines show the best-fit evolutionary trend of M_{BH}/M_* and 1σ errors at $z < 2$ (McLure et al. 2006). The gray area shows the typical range of $M_{\text{BH}}/M_* \sim 0.002\text{--}0.005$ in the local Universe (Kormendy & Ho 2013).

5.6. Estimation of the Central Supermassive Black Hole Mass and Growth Rate

Recent studies of Hot DOGs have consistently revealed that their Eddington ratios are near or above the Eddington limit (Wu et al. 2018; Finnerty et al. 2020; Jun et al. 2020). Tsai et al. (2018) reported the measurement of M_{BH} of W2246–0526. By using the L_{AGN} of W2246–0526 from our SED fitting, we estimated a super-Eddington ratio $\lambda_{\text{Edd}} = L_{\text{AGN}}/L_{\text{Edd}} = 1.7$, where $L_{\text{Edd}}/L_{\odot} = 3.28 \times 10^4 (M_{\text{BH}}/M_{\odot})$. Given these studies, we assume an Eddington ratio $\lambda_{\text{Edd}} = 1.0$ for our Hot DOG sample and infer the mass of the SMBH M_{BH} and the black hole to stellar mass ratio M_{BH}/M_* . The results are listed in Table 7.

In Figure 9, we plot M_{BH}/M_* as a function of redshift for the Hot DOGs and other samples of AGN for different redshift and AGN bolometric luminosity ranges. Similar to other luminous quasars at redshift 2–4 (e.g., Targett et al. 2012; Trakhtenbrot et al. 2015; Matsuoka et al. 2018), the inferred M_{BH}/M_* of the Hot DOG sample is about 2 times higher than the evolutionary trend of M_{BH}/M_* seen by McLure et al. (2006). Bischetti et al. (2021) also revealed an extremely high ratio between SMBH mass and dynamical mass $M_{\text{BH}}/M_{\text{dyn}}$ in WISSH quasars. These WISSH quasars also exhibit a close or super unit Eddington ratio. In contrast, obscured and unobscured AGN with moderate AGN bolometric luminosities at redshifts 1–2 (e.g., Merloni et al. 2010; Bongiorno et al. 2014) exhibit a relatively low M_{BH}/M_* value. Using the equation $L_{\text{AGN}} = (\eta \dot{M}_{\text{BH}} c^2)/(1 - \eta)$ and adopting $\frac{\eta}{1 - \eta} = 0.1$, we derived high black hole growth rates of $\dot{M}_{\text{BH}} \sim 65^{+39}_{-29} M_{\odot} \text{ yr}^{-1}$ for our sample. These results suggest rapid black hole growth in Hot DOGs, consistent with Wu et al. (2018). During this high-accretion phase, the majority of the black hole mass could be assembled within the Salpeter

timescale, which is consistent with the gas depletion timescale and the high luminosity state timescale measured in Tsai et al. (2015).

6. Summary and Conclusion

We present a UV to millimeter SED analysis and molecular gas content measurements in a sample of 16 WISE-selected, hyperluminous dust-obscured quasars at $z \sim 3$. We inferred the physical properties of this sample, such as the gas-to-dust ratio, molecular gas fraction, and SFE. This study represents the largest sample to date in which a systematic investigation of the cold gas content in hyperluminous quasars at Cosmic Noon has been conducted. The main results can be summarized as follows:

1. Based on ALMA observations of the CO(3–2) and CO(4–3) lines, we have calculated the average molecular gas mass $M_{\text{H}_2} = 3.69_{-2.61}^{+9.92} \times 10^{10} M_{\odot}$ of our sample by adopting $L'_{\text{CO}(3-2)}/L'_{\text{CO}(1-0)} = 0.97$, $L'_{\text{CO}(4-3)}/L'_{\text{CO}(1-0)} = 0.87$, and $\alpha_{\text{CO}} = 0.8 M_{\odot} (\text{K km s}^{-1} \text{ pc}^2)^{-1}$. The derived molecular gas masses are higher than the prediction in Fan et al. (2016b).
2. We modeled the observed UV to millimeter SEDs of our sample using an updated version of BayeSED. The median values and 16th–84th quartiles of all sources in our sample are given as follows. For the cold dust emission represented by the graybody function, we estimated a typical $T_{\text{dust}} \sim 45_{-1}^{+2} \text{ K}$, $\beta \sim 2.5_{-0.2}^{+0.2}$, $L_{\text{IR}} \sim 1.1_{-0.3}^{+1.3} \times 10^{13} L_{\odot}$, and $M_{\text{dust}} = 8.0_{-4.8}^{+4.0} \times 10^7 M_{\odot}$. For the stellar component, we inferred a typical $M_{\star} \sim 5.8_{-2.3}^{+12.3} \times 10^{10} M_{\odot}$ and $\text{SFR} \sim 1008_{-409}^{+597} M_{\odot} \text{ yr}^{-1}$. For the AGN component, we obtained a typical $L_{\text{AGN}} \sim 9.7_{-4.3}^{+5.8} \times 10^{13} L_{\odot}$.
3. We estimated the gas-to-dust ratio, finding $\delta_{\text{GDR}} \sim 474_{-324}^{+711}$. Most Hot DOGs in our sample exhibited a higher δ_{GDR} than the typical values for the Milky Way, local star-forming galaxies, and high-redshift SMGs. This discrepancy can potentially be attributed to the intense radiation field and high dust temperatures caused by starbursts and potentially the central AGNs, which may result in an underestimation of M_{dust} .
4. We inferred the molecular gas fraction, finding $f_{\text{gas}} \sim 0.33_{-0.17}^{+0.33}$. By comparing our findings with SMGs, obscured quasars from the literature, and the $f_{\text{gas}}-z$ relation for MS galaxies, we found that Hot DOGs exhibit a relatively low gas content. This lower gas content is likely attributed to the depletion of gas caused by AGN-driven outflows.
5. The remarkable offset of our Hot DOGs from the MS, $\Delta_{\text{MS}} \sim 6.12_{-2.9}^{+5.1}$, suggests that the majority of our Hot DOGs are extreme starburst systems. The gas depletion timescales, $39_{-28}^{+85} \text{ Myr}$, are remarkably short. When comparing the average SFE $\sim 297_{-195}^{+659} \text{ K km s}^{-1} \text{ pc}^{-2}$ with those of SMGs, obscured and unobscured quasars, as well as MS galaxies, we found that Hot DOGs exhibit higher SFEs, similar to optically luminous quasars and obscured quasars, rather than SMGs and MS galaxies. Moreover, we discovered a positive correlation between SFE and AGN bolometric luminosity.

6. Based on AGN bolometric luminosity, we inferred a typical black hole growth rate $\sim 65_{-29}^{+39} M_{\odot} \text{ yr}^{-1}$ and a typical black hole mass $\sim 3.0_{-1.3}^{+1.8} \times 10^9 M_{\odot}$ by adopting $\frac{\eta}{1-\eta} = 0.1$ and $\lambda_{\text{Edd}} = 1.0$, respectively. These results suggest that the majority of the black hole mass can be assembled within a Salpeter timescale, which is consistent with the gas depletion timescale and the high luminosity state timescale of Hot DOGs suggested by Tsai et al. (2015). The observed black hole to stellar mass ratio $\sim 0.042_{-0.026}^{+0.029}$ is similar to other high-redshift luminous quasars.

We conclude that our results are consistent with the scenario that our sample represents a phase when both star formation and AGN activity are at their peak, leading to rapid depletion of gas and dust, ultimately transiting the galaxies toward unobscured quasars.

Acknowledgments




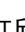
We thank the anonymous referee for constructive comments and suggestions. This work is supported by National Key Research and Development Program of China (2023YFA1608100) and the Strategic Priority Research Program of Chinese Academy of Sciences, grant No. XDB 41000000. L.F. gratefully acknowledges the support of the National Natural Science Foundation of China (NSFC; grant Nos. 12173037 and 12233008), the CAS Project for Young Scientists in Basic Research (No. YSBR-092), the China Manned Space Project (No. CMS-CSST-2021-A04 and No. CMS-CSST-2021-A06), the Fundamental Research Funds for the Central Universities (WK3440000006), Cyrus Chun Ying Tang Foundations, and the 111 Project for “Observational and Theoretical Research on Dark Matter and Dark Energy” (B23042). Y.K. acknowledges the support of the NSFC (grant Nos. 11773063 and 12288102), the “Light of West China” Program of the Chinese Academy of Sciences, and the Yunnan Ten Thousand Talents Plan Young & Elite Talents Project. We thank the staff of the Nordic ALMA Regional Center node for their support and helpful discussions. K.K. acknowledges support from the Swedish Research Council and the Knut and Alice Wallenberg Foundation. This paper makes use of the following ALMA data: ADS/JAO.ALMA#2017.1.00441.S and ADS/JAO.ALMA#2017.1.00358.S. ALMA is a partnership of ESO (representing its member states), NSF (USA), and NINS (Japan), together with NRC (Canada), NSC and ASIAA (Taiwan), and KASI (Republic of Korea), in cooperation with the Republic of Chile. The Joint ALMA Observatory is operated by ESO, AUI/NRAO, and NAOJ.

Based on observations made with ESO Telescopes at the La Silla Paranal Observatory under program IDs 177.A-3016, 177.A-3017, 177.A-3018, and 179.A-2004, and on data products produced by the KiDS consortium. The KiDS production team acknowledges support from Deutsche Forschungsgemeinschaft, ERC, NOVA, and NWO-M grants; Target; the University of Padova; and the University Federico II (Naples).

Facility: ALMA, WISE, Herschel (PACS, SPIRE), CTIO (DECam), Paranal (OmegaCam, VISTA), Bok (90prime), and SDSS.

ORCID iDs

Weibin Sun (孙卫斌)  <https://orcid.org/0009-0004-7885-5882>
Lulu Fan (范璐璐)  <https://orcid.org/0000-0003-4200-4432>

Yunkun Han (韩云坤)  <https://orcid.org/0000-0002-2547-0434>
 Kirsten K. Knudsen  <https://orcid.org/0000-0002-7821-8873>
 Guangwen Chen (陈广文)  <https://orcid.org/0000-0002-4742-8800>
 Hong-Xin Zhang (张红欣)  <https://orcid.org/0000-0003-1632-2541>

References

- Abbott, T. M. C., Abdalla, F. B., Allam, S., et al. 2018, *ApJS*, **239**, 18
- Alonso-Herrero, A., García-Burillo, S., Hönig, S. F., et al. 2021, *A&A*, **652**, A99
- Aravena, M., Bertoldi, F., Schinnerer, E., et al. 2008, *A&A*, **491**, 173
- Assef, R. J., Bauer, F. E., Blain, A. W., et al. 2022, *ApJ*, **934**, 101
- Assef, R. J., Brightman, M., Walton, D. J., et al. 2020, *ApJ*, **897**, 112
- Assef, R. J., Eisenhardt, P. R. M., Stern, D., et al. 2015, *ApJ*, **804**, 27
- Assef, R. J., Walton, D. J., Brightman, M., et al. 2016, *ApJ*, **819**, 111
- Banerji, M., Carilli, C. L., Jones, G., et al. 2017, *MNRAS*, **465**, 4390
- Berta, S., Lutz, D., Santini, P., et al. 2013, *A&A*, **551**, A100
- Bischetti, M., Feruglio, C., Piconcelli, E., et al. 2021, *A&A*, **645**, A33
- Bischetti, M., Piconcelli, E., Feruglio, C., et al. 2019, *A&A*, **628**, A118
- Bolatto, A. D., Wolfire, M., & Leroy, A. K. 2013, *ARA&A*, **51**, 207
- Bongiorno, A., Maiolino, R., Brusa, M., et al. 2014, *MNRAS*, **443**, 2077
- Boquien, M., Burgarella, D., Roehlly, Y., et al. 2019, *A&A*, **622**, A103
- Bothwell, M. S., Smail, I., Chapman, S. C., et al. 2013, *MNRAS*, **429**, 3047
- Brusa, M., Cresci, G., Daddi, E., et al. 2018, *A&A*, **612**, A29
- Brusa, M., Feruglio, C., Cresci, G., et al. 2015, *A&A*, **578**, A11
- Bruzual, G., & Charlot, S. 2003, *MNRAS*, **344**, 1000
- Buat, V., Heinis, S., Boquien, M., et al. 2014, *A&A*, **561**, A39
- Calzetti, D., Armus, L., Bohlin, R. C., et al. 2000, *ApJ*, **533**, 682
- Carilli, C. L., & Walter, F. 2013, *ARA&A*, **51**, 105
- Chabrier, G. 2003, *PASP*, **115**, 763
- Conroy, C. 2013, *ARA&A*, **51**, 393
- Cutri, R. M., Wright, E. L., Conrow, T., et al. 2013, *yCat*, **II/328**
- da Cunha, E., Charlot, S., & Elbaz, D. 2008, *MNRAS*, **388**, 1595
- Dey, A., Schlegel, D. J., Lang, D., et al. 2019, *AJ*, **157**, 168
- Díaz-Santos, T., Assef, R. J., Blain, A. W., et al. 2016, *ApJL*, **816**, L6
- Díaz-Santos, T., Assef, R. J., Blain, A. W., et al. 2018, *Sci*, **362**, 1034
- Díaz-Santos, T., Assef, R. J., Eisenhardt, P. R. M., et al. 2021, *A&A*, **654**, A37
- Draine, B. T. 2003, *ARA&A*, **41**, 241
- Draine, B. T., Dale, D. A., Bendo, G., et al. 2007, *ApJ*, **663**, 866
- Draine, B. T., & Li, A. 2007, *ApJ*, **657**, 810
- Drouart, G., De Breuck, C., Vernet, J., et al. 2014, *A&A*, **566**, A53
- Dunne, L., Eales, S., Ivison, R., Morgan, H., & Edmunds, M. 2003, *Natur*, **424**, 285
- Duras, F., Bongiorno, A., Piconcelli, E., et al. 2017, *A&A*, **604**, A67
- Duras, F., Bongiorno, A., Ricci, F., et al. 2020, *A&A*, **636**, A73
- Edge, A., Sutherland, W., Kuijken, K., et al. 2013, *Mnscr*, **154**, 32
- Eisenhardt, P. R. M., Wu, J., Tsai, C.-W., et al. 2012, *ApJ*, **755**, 173
- Fabian, A. C. 2012, *ARA&A*, **50**, 455
- Fan, L., Gao, Y., Knudsen, K. K., et al. 2018, *ApJ*, **854**, 157
- Fan, L., Han, Y., Fang, G., et al. 2016a, *ApJL*, **822**, L32
- Fan, L., Han, Y., Nikutta, R., Drouart, G., & Knudsen, K. K. 2016b, *ApJ*, **823**, 107
- Fan, L., Jones, S. F., Han, Y., & Knudsen, K. K. 2017, *PASP*, **129**, 124101
- Fan, L., Knudsen, K. K., Fogasy, J., et al. 2018, *ApJL*, **856**, L5
- Fan, L., Knudsen, K. K., Han, Y., et al. 2019, *ApJ*, **887**, 74
- Faucher-Giguère, C.-A., & Quataert, E. 2012, *MNRAS*, **425**, 605
- Ferrarese, L., & Ford, H. 2005, *SSRv*, **116**, 523
- Feruglio, C., Ferrara, A., Bischetti, M., et al. 2017, *A&A*, **608**, A30
- Finnerty, L., Larson, K., Soifer, B. T., et al. 2020, *ApJ*, **905**, 16
- Fiore, F., Feruglio, C., Shankar, F., et al. 2017, *A&A*, **601**, A143
- Fluetsch, A., Maiolino, R., Carniani, S., et al. 2019, *MNRAS*, **483**, 4586
- Fritz, J., Franceschini, A., & Hatziminaoglou, E. 2006, *MNRAS*, **366**, 767
- García-Burillo, S., Alonso-Herrero, A., Ramos Almeida, C., et al. 2021, *A&A*, **652**, A98
- Genzel, R., Tacconi, L. J., Gracia-Carpio, J., et al. 2010, *MNRAS*, **407**, 2091
- Ginolfi, M., Piconcelli, E., Zappacosta, L., et al. 2022, *NatCo*, **13**, 4574
- González-Martín, O., Masegosa, J., García-Bernete, I., et al. 2019, *ApJ*, **884**, 11
- Griffin, M. J., Abergel, A., Abreu, A., et al. 2010, *A&A*, **518**, L3
- Han, Y., Fan, L., Zheng, X. Z., et al. 2023, *ApJS*, **269**, 39
- Han, Y., & Han, Z. 2012, *ApJ*, **749**, 123
- Han, Y., & Han, Z. 2014, *ApJS*, **215**, 2
- Han, Y., & Han, Z. 2019, *ApJS*, **240**, 3
- Heckman, T. M., & Best, P. N. 2014, *ARA&A*, **52**, 589
- Hickox, R. C., & Alexander, D. M. 2018, *ARA&A*, **56**, 625
- Hönig, S. F., & Kishimoto, M. 2010, *A&A*, **523**, A27
- Hönig, S. F., & Kishimoto, M. 2017, *ApJL*, **838**, L20
- Hopkins, P. F., Hernquist, L., Cox, T. J., et al. 2008, *ApJS*, **175**, 356
- Hopkins, P. F., Torrey, P., Faucher-Giguère, C.-A., et al. 2016, *MNRAS*, **458**, 816
- Ichikawa, K., Packham, C., Ramos Almeida, C., et al. 2015, *ApJ*, **803**, 57
- James, A., Dunne, L., Eales, S., & Edmunds, M. G. 2002, *MNRAS*, **335**, 753
- Jenkins, E. B. 2004, in *Origin and Evolution of the Elements*, ed. A. McWilliam & M. Rauch (Cambridge: Cambridge Univ. Press), 336
- Jones, A. P. 2004, in *ASP Conf. Ser. 309, Astrophysics of Dust*, ed. A. N. Witt, G. Clayton, & B. T. Draine (San Francisco, CA: ASP), 347
- Jones, S. F., Blain, A. W., Assef, R. J., et al. 2017, *MNRAS*, **469**, 4565
- Jones, S. F., Blain, A. W., Lonsdale, C., et al. 2015, *MNRAS*, **448**, 3325
- Jones, S. F., Blain, A. W., Stern, D., et al. 2014, *MNRAS*, **443**, 146
- Jun, H. D., Assef, R. J., Bauer, F. E., et al. 2020, *ApJ*, **888**, 110
- Kakkad, D., Mainieri, V., Brusa, M., et al. 2017, *MNRAS*, **468**, 4205
- Kennicutt, R. C. 1998, *ARA&A*, **36**, 189
- Komatsu, E., Smith, K. M., Dunkley, J., et al. 2011, *ApJS*, **192**, 18
- Kormendy, J., & Ho, L. C. 2013, *ARA&A*, **51**, 511
- Kuijken, K., Heymans, C., Dvornik, A., et al. 2019, *A&A*, **625**, A2
- Lang, D. 2014, *AJ*, **147**, 108
- Li, G., Tsai, C.-W., Stern, D., et al. 2023, *ApJ*, **958**, 162
- Liang, L., Feldmann, R., Kereš, D., et al. 2019, *MNRAS*, **489**, 1397
- López, I. E., Brusa, M., Bonoli, S., et al. 2023, *A&A*, **672**, A137
- Luo, Y., Fan, L., Zou, H., et al. 2022, *ApJ*, **935**, 80
- Lyu, J., & Rieke, G. H. 2018, *ApJ*, **866**, 92
- Magnelli, B., Lutz, D., Santini, P., et al. 2012, *A&A*, **539**, A155
- Magorrian, J., Tremaine, S., Richstone, D., et al. 1998, *AJ*, **115**, 2285
- Marasco, A., Cresci, G., Nardini, E., et al. 2020, *A&A*, **644**, A15
- Matsuoka, K., Toba, Y., Shidatsu, M., et al. 2018, *A&A*, **620**, L3
- McLure, R. J., Jarvis, M. J., Targett, T. A., et al. 2006, *MNRAS*, **368**, 1395
- McMullin, J. P., Waters, B., Schiebel, D., Young, W., & Golap, K. 2007, *adass* **XVI**, 376, 127
- Meisner, A. M., Lang, D., & Schlegel, D. J. 2017, *AJ*, **154**, 161
- Merloni, A., Bongiorno, A., Bolzonella, M., et al. 2010, *ApJ*, **708**, 137
- Miettinen, O., Delvecchio, I., Smolčić, V., et al. 2017, *A&A*, **606**, A17
- Mihos, J. C., & Hernquist, L. 1996, *ApJ*, **464**, 641
- Nenkova, M., Sirocky, M. M., Ivezić, Ž., & Elitzur, M. 2008a, *ApJ*, **685**, 147
- Nenkova, M., Sirocky, M. M., Nikutta, R., Ivezić, Ž., & Elitzur, M. 2008b, *ApJ*, **685**, 160
- Netzer, H. 2015, *ARA&A*, **53**, 365
- Noguchi, M., & Ishibashi, S. 1986, *MNRAS*, **219**, 305
- Ossenkopf, V., Henning, T., & Mathis, J. S. 1992, *A&A*, **261**, 567
- Penney, J. I., Blain, A. W., Assef, R. J., et al. 2020, *MNRAS*, **496**, 1565
- Penney, J. I., Blain, A. W., Wylezalek, D., et al. 2019, *MNRAS*, **483**, 514
- Perna, M., Sargent, M. T., Brusa, M., et al. 2018, *A&A*, **619**, A90
- Piconcelli, E., Vignali, C., Bianchi, S., et al. 2015, *A&A*, **574**, L9
- Pier, E. A., & Krolik, J. H. 1993, *ApJ*, **418**, 673
- Pilbratt, G. L., Riedinger, J. R., Passvogel, T., et al. 2010, *A&A*, **518**, L1
- Poglitsch, A., Waelkens, C., Geis, N., et al. 2010, *A&A*, **518**, L2
- Pozzi, F., Calura, F., Fudamoto, Y., et al. 2021, *A&A*, **653**, A84
- Ramos Almeida, C., & Ricci, C. 2017, *NatAs*, **1**, 679
- Rémy-Ruyer, A., Madden, S. C., Galliano, F., et al. 2014, *A&A*, **563**, A31
- Ricci, C., Assef, R. J., Stern, D., et al. 2017, *ApJ*, **835**, 105
- Roseboom, I. G., Ivison, R. J., Greve, T. R., et al. 2012, *MNRAS*, **419**, 2758
- Sanders, D. B., Soifer, B. T., Elias, J. H., et al. 1988, *ApJ*, **325**, 74
- Sargent, M. T., Daddi, E., Béthermin, M., et al. 2014, *ApJ*, **793**, 19
- Schneider, R., Bianchi, S., Valiante, R., et al. 2015, *A&A*, **579**, A60
- Scoville, N., Murchikova, L., Walter, F., et al. 2017, *ApJ*, **836**, 66
- Shangguan, J., Ho, L. C., Bauer, F. E., et al. 2020, *ApJ*, **899**, 112
- Shapley, A. E. 2011, *ARA&A*, **49**, 525
- Siebenmorgen, R., Heymann, F., & Efstathiou, A. 2015, *A&A*, **583**, A120
- Siebenmorgen, R., Voshchinnikov, N. V., & Bagnulo, S. 2014, *A&A*, **561**, A82
- Silva, A., Sajina, A., Lonsdale, C., et al. 2015, *ApJL*, **806**, L25
- Sokol, A. D., Yun, M., Pope, A., et al. 2023, *MNRAS*, **521**, 818
- Solomon, P. M., & Vanden Bout, P. A. 2005, *ARA&A*, **43**, 677
- Somerville, R. S., & Davé, R. 2015, *ARA&A*, **53**, 51
- Sommovigo, L., Ferrara, A., Pallottini, A., et al. 2020, *MNRAS*, **497**, 956
- Speagle, J. S., Steinhardt, C. L., Capak, P. L., et al. 2014, *ApJS*, **214**, 15
- Stalevski, M., Ricci, C., Ueda, Y., et al. 2016, *MNRAS*, **458**, 2288
- Stern, D., Lansbury, G. B., Assef, R. J., et al. 2014, *ApJ*, **794**, 102
- Suh, H., Civano, F., Hasinger, G., et al. 2019, *ApJ*, **872**, 168
- Targett, T. A., Dunlop, J. S., & McLure, R. J. 2012, *MNRAS*, **420**, 3621

- Toba, Y., & Nagao, T. 2016, [ApJ](#), **820**, 46
- Trakhtenbrot, B., Urry, C. M., Civano, F., et al. 2015, [Sci](#), **349**, 168
- Tripodi, R., Feruglio, C., Kemper, F., et al. 2023, [ApJL](#), **946**, L45
- Tsai, C.-W., Eisenhardt, P. R. M., Jun, H. D., et al. 2018, [ApJ](#), **868**, 15
- Tsai, C.-W., Eisenhardt, P. R. M., Wu, J., et al. 2015, [ApJ](#), **805**, 90
- Tsukui, T., Wisnioski, E., Krumholz, M. R., et al. 2023, [MNRAS](#), **523**, 4654
- Vito, F., Brandt, W. N., Stern, D., et al. 2018, [MNRAS](#), **474**, 4528
- Weymann, R. J., Morris, S. L., Foltz, C. B., et al. 1991, [ApJ](#), **373**, 23
- Wright, E. L., Eisenhardt, P. R. M., Mainzer, A. K., et al. 2010, [AJ](#), **140**, 1868
- Wu, J., Bussmann, R. S., Tsai, C.-W., et al. 2014, [ApJ](#), **793**, 8
- Wu, J., Jun, H. D., Assef, R. J., et al. 2018, [ApJ](#), **852**, 96
- Wu, J., Tsai, C.-W., Sayers, J., et al. 2012, [ApJ](#), **756**, 96
- Yang, G., Boquien, M., Brandt, W. N., et al. 2022, [ApJ](#), **927**, 192
- Zappacosta, L., Piconcelli, E., Duras, F., et al. 2018, [A&A](#), **618**, A28
- Zewdie, D., Assef, R. J., Mazzucchelli, C., et al. 2023, [A&A](#), **677**, A54
- Zou, H., Zhou, X., Fan, X., et al. 2019, [ApJS](#), **245**, 4